Modelling Heavy Elements in a Dynamic Chromosphere

Stefano Pucci
Master's thesis
Institute of Theoretical Astrophysics
University of Oslo

December 2008

Preface

This thesis is the result from a collaboration between Iselin Bø and the undersigned, under the supervising of Øystein Lie-Svendsen. The collaboration concerns in particular the implementation of the numerical model. This is why the chapters 2 and 3, which describe the physical problem and the work with the code, are in common, i.e. are included in both the theses. However, the section 2.1.1, concerning the radiative ionisation, describes an approach that differs from Bø's thesis.

Once the main body of the code has been built, the two works have followed different paths.

The undersigned have studied a dynamic chromospheric layer with the aim to investigate the abundance variation in the fast solar wind. Bø has instead focused on the element fractionation resulting from a gravitational settling in a chromosphere without any net outflow of hydrogen.

I would like to thank my supervisor Øystein Lie-Svendsen for the innumerable hours he dedicated to guide me through this project. Thanks also to Tara and Kosovare for proof reading this thesis, and special thanks to "nonne" Giovannella and Kirsten and "zia" Lilja. Finally great thanks to Erika that reminded us of the importance of Astrophysics in our lives.

Oslo, December 2008

Stefano Pucci

Contents

1 Introduction **1**
- 1.1 Observations . . . 2
- 1.2 Models . . . 7
- 1.3 The present work . . . 8

2 The model **9**
- 2.1 Ionisation rates . . . 11
  - 2.1.1 Radiative Ionisation . . . 11
  - 2.1.2 Collisional ionisation . . . 12
- 2.2 Recombination rates . . . 13
  - 2.2.1 Radiative recombination for hydrogen . . . 13
  - 2.2.2 Recombination rates for the minor constituents . . . 14
  - 2.2.3 Dielectronic recombination rate for iron . . . 14
- 2.3 Charge transfer . . . 14
- 2.4 Electric field . . . 16
- 2.5 Collisions . . . 16
  - 2.5.1 Neutral-neutral collisions . . . 17
  - 2.5.2 Neutral-ion collisions . . . 17
  - 2.5.3 Ion-ion collisions . . . 18

3 The numerical model **21**
- 3.1 Double grid . . . 21
- 3.2 Semi-implicit scheme . . . 22
- 3.3 Newton-Raphson method . . . 24
- 3.4 Boundary conditions . . . 26

4 The ionisation-diffusion model of Peter **29**

5 The hydrogen background **33**
- 5.1 Boundary conditions . . . 34
- 5.2 Results . . . 34

5.3 Discussion 41

6 The minor constituents **45**
6.1 Boundary conditions 45
6.2 Oxygen 46
6.2.1 Results 46
6.2.2 Discussion 51
6.3 Low FIP elements 53
6.3.1 Silicon 53
6.3.2 Magnesium 55
6.3.3 Iron 60
6.3.4 Discussion 62
6.4 Neon 63
6.4.1 Results 63
6.4.2 Discussion 68

7 Discussion **69**
7.1 The background model 69
7.2 The minor constituents model 69
7.2.1 Searching for enrichment 69
7.2.2 Additional results 74
7.2.3 Gradual ionisation 79

8 Summary **81**

Bibliography **82**

Chapter 1

Introduction

Elemental abundance in the photosphere is believed to be homogeneous, and to represent the same abundance as the proto-nebula that formed the solar system (Feldman and Laming, 2000). The high density and the strong convection, in fact, leads to a well mixed photosphere.

However the composition of the upper atmosphere presents some significant variations from the photosphere. Furthermore different structures in the corona and in solar wind show different abundances. Both in-situ measurements of solar wind and spectroscopic measurements of the coronal spectrum provide evidence for a different level of abundance between the photosphere and the upper atmosphere.

In the upper atmosphere the elements with a low *First Ionisation Potential* ($FIP \leq 10$eV) are enriched relative to high *FIP* elements and with respect to the photospheric ratio.

This *FIP effect* can be quantified defining the relative and absolute fractionation for a generic element x:

$$(f_{abs})_x^{structure} = \frac{(A_{abs})^{structure}}{(A_{abs})^{photosphere}} \tag{1.1}$$

and

$$(f_{rel})_x^{structure} = \frac{(A_{rel})^{structure}}{(A_{rel})^{photosphere}} \ , \tag{1.2}$$

where the *absolute* and *relative abundances* are defined as:

$$A_{abs} = \frac{N_x}{N_H} \tag{1.3}$$

and

$$A_{rel} = \frac{N_x}{N_O}, \tag{1.4}$$

	FIP(eV)	$\log A_x$	N_x/N_H
H	13.6	12.00	1
O	13.6	8.66 ± 0.05 [1]	$(4.07 - 5.13) \times 10^{-4}$
Ne	21.6	8.08 ± 0.06	$(1.05 - 1.38) \times 10^{-4}$
Mg	7.6	7.58 ± 0.05	$(3.39 - 4.27) \times 10^{-5}$
Si	8.1	7.55 ± 0.05	$(3.16 - 3.98) \times 10^{-5}$
Fe	7.9	7.50 ± 0.05	$(2.82 - 3.55) \times 10^{-5}$

Table 1.1: *Photospheric abundances and first ionisation potentials for selected elements (Grevesse and Sauval, 1998).*

where N_X is the total density of the considered element, N_H and N_O are the total hydrogen density and the total oxygen density.

This work will focus on the solar wind abundance variations.

1.1 Observations

The elemental abundances of the photosphere have been studied since 1929, when Russell (1929) analysed the spectrum of the solar photosphere and determined the abundances of 56 elements. Since then many measurements have been done and the different elemental abundances are now believed to be well known. The only exception is represented by oxygen, for which the measured abundance has decreased by a factor of 0.46 from measurements in 1989 to 2004 (Asplund et al., 2004).

The elemental abundances for the photosphere are shown in table 1.1. These values are given both in the standard logarithmic scale $\log A_x = 12 + \log_{10}(N_x/N_H)$ and as a simple density ratio, and are obtained by spectroscopic measurements (Grevesse and Sauval, 1998).

To quantify the intensity of a line we can measure the *equivalent width*, which is related to the area between the line and the continuum intensity, in a plot of the intensity versus the wavelength. How the equivalent width increases with gas density is described by the *curve of growth* (Gray, 2005). Thus, by measuring the equivalent width and calculating the curve of growth, we can get an estimate for the density of the gas. The curve of growth is related to many model parameters like temperature and levels population, but also to atomic-physics quantities like transition probability. Hence obtaining a good estimate of elemental abundances from the line strength requires detailed models to describe both the solar atmosphere and the physics of the

[1] The oxygen abundance is taken from Asplund et al. (2004)

transitions.

Another method to obtain an estimate of the photospheric abundances consists of measuring the composition of a special kind of meteorite (CI carbonaceous chondrites). These meteorites are believed to come from asteroids that were not subject to the differentiation processes that affected the planet formation and thus are characterised by the same composition of the proto-nebula that formed the solar system. The chondrites abundance values confirm the spectroscopic values listed in table 1.1. This comparison is obviously legitimated only for non-volatile elements, i.e. in our case for magnesium, silicon and iron.

While the photosphere is characterised by a homogeneous and constant composition, different structures of the upper atmosphere and solar wind present important variations in the compositions. We will now focus on solar wind measurements.

The spacecraft Ulysses was the first satellite to complete a polar orbit (inclination 80.22°) around the sun. A review of the studies from Ulysses measurements of the solar wind composition can be found in von Steiger and Schwadron (2000). Measurements from the SWICS (Solar Wind Ion Composition Spectrometer) instrument on board Ulysses confirm that the solar wind is mainly made up of two fundamentally different components: fast wind and slow wind.

Fast solar wind is characterised by high velocities (≈ 750 km s^{-1} measured at 1 AU) and a ratio between the charge states of a specific element (called the freezing-in temperature) that reflects the coronal electron temperature above coronal hole regions (Feldman and Laming, 2000). There is in fact quite good agreement on the source location of fast wind in the coronal holes. Coronal holes are regions where the coronal plasma is colder and characterised by a density lower than the typical values of temperature and density in the corona. Normally coronal holes are located over the sun poles, but during high activity periods coronal holes can extend to lower latitude regions and causing fast solar wind to mix with slow wind in the ecliptic plane.

Slow solar wind is characterised by lower velocities (≈ 400 km s^{-1} measured at 1 AU), and different from fast wind, no single electron temperature can describe the spectra of elements (von Steiger and Schwadron, 2000). Slow solar wind seems to originate from quiet coronal regions but there is no full agreement upon its origin. Abundances comparison can suggest the coronal loops as sources for slow wind, but this requires that these loops have to open to release the plasma.

A third component of solar wind, associated with transient phenomena, appears during high activity periods and is called the Solar Energetic Particle event.

Because of the much larger hydrogen abundance relative to the rest of the solar abundant elements, it is easier to use another element (oxygen in most cases) for comparisons. In order to give an absolute meaning to these comparisons the hydrogen abundance relative to oxygen (or vice versa) is needed. With the SWICS instrument, the obtained hydrogen relative abundance value (N_H/N_O) is: $A_{rel} = 1890 \pm 600$ in slow wind and $A_{rel} = 1590 \pm 500$ in fast wind (von Steiger et al., 1995). With the photospheric value for the hydrogen relative abundance given by Asplund et al. (2004), $A_{rel} = 2190 \pm 250$, both slow and fast wind value are inside the uncertainty. Moreover the adopted value for the hydrogen relative abundance in the photosphere has been subject to numerous corrections in the last years (see also Grevesse and Sauval (1998)). Hence, there is no experimental evidence of an absolute fractionation for oxygen.

The SWICS instrument could measure and characterise the incoming ions determining the energy per charge and the mass per charge. In that way the instrument could perform comparable measurements of elemental abundances relative to wind velocity. A sample of these measurements, averaged over a 5-days period, is presented in Fig. 1.1. The green periods sample shows slow wind, measuring when Ulysses was passing at low latitudes ($< 15°$), whereas the purple sample shows fast wind measuring over the South Pole. The low FIP element silicon presents a relative abundance that is higher in slow wind than in fast wind. For the medium FIP element carbon the picture is quite different with no significant variations between slow and fast wind. Another observation is that both of the relative abundances are more variable in slow wind than in fast wind.

Fig. 1.2 shows relative fractionation values measured by SWICS, averaged over two periods for a total of ≈ 600 days, for both fast and slow wind. In slow wind (upper panel) the fractionation for low FIP elements (magnesium, silicon, and iron), is a bit less than 3 and the medium FIP (sulphur and carbon) are also enriched by a factor of ≈ 1.5. The high FIP element nitrogen and neon and the very high FIP helium are depleted relative to oxygen.

In fast wind the low FIP elements are still enriched but just by a factor of ≈ 2 and the medium FIP elements are enhanced by approximately the same factor as in slow wind. Nitrogen presents almost no depletion whereas neon and helium are still quite depleted.

Another difference between slow and fast wind, as already pointed, is the variability of the values: the fractionation values in the fast wind are much less variable than the respective values in slow wind.

These results changed the canonical picture of the FIP effect in solar wind. Previous measurements, made by satellites with low inclined orbits (see Table 1 from von Steiger and Geiss (1989) for a review), gave an enrichment

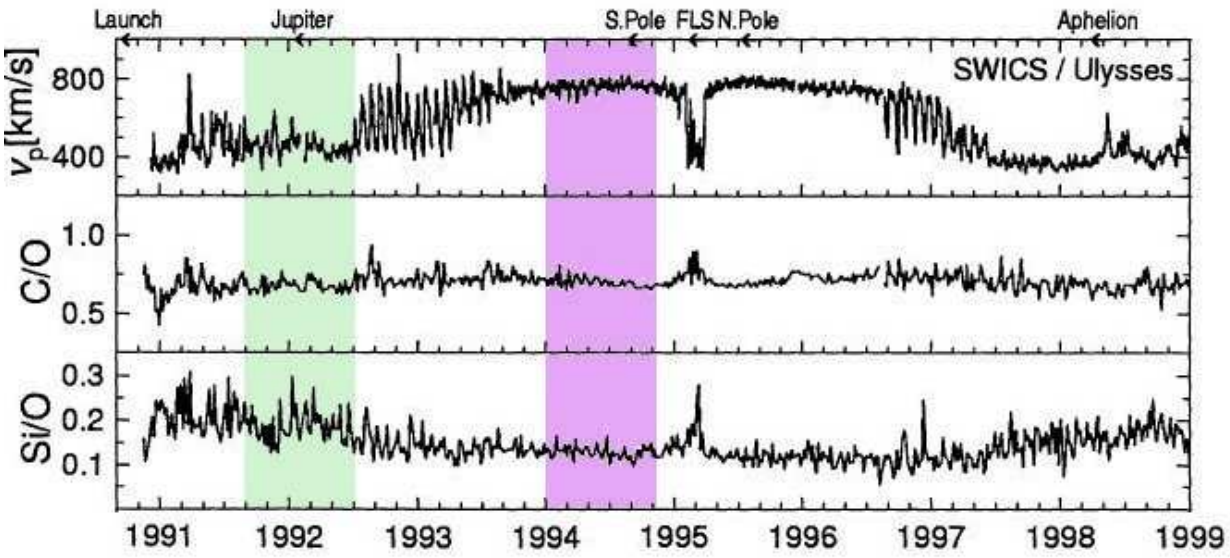

Figure 1.1: *5-days averaged values for silicon relative abundance (lower panel) and carbon relative abundance (middle panel) from SWICS instrument in comparison to the solar wind speed of protons from SWOOPS (Solar Winds Observations Over the Poles of the Sun) instrument (upper panel). Figure adapted from von Steiger and Schwadron (2000).*

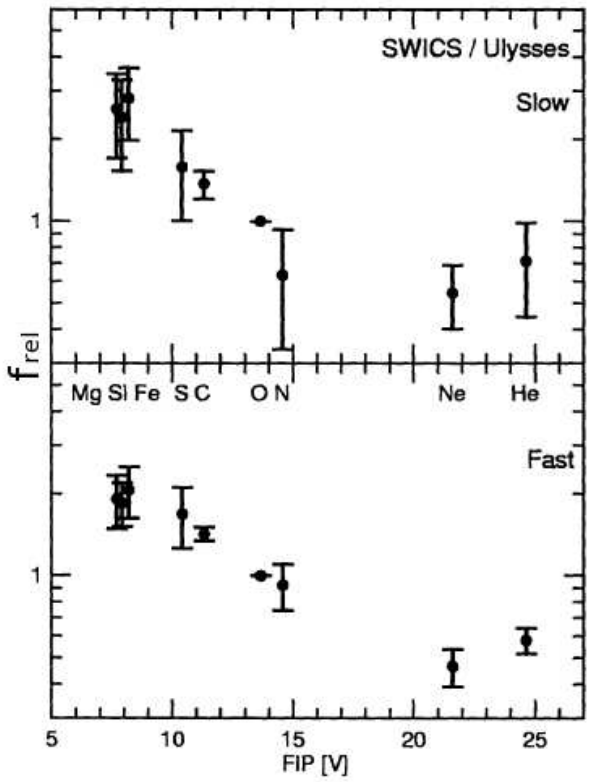

Figure 1.2: *600-days averaged values for relative fractionation (see eq. 1.2) plotted versus the ionisation potential. The points represent the averaged values and the error bars denotes the natural variability of the daily values. Figure adapted from von Steiger and Schwadron (2000).*

of low FIP between 3.5 and 5 in slow wind, while almost no enrichment was measured for the low FIP elements in the fast wind. Yet FIP elements were observed to present no depletion relative to oxygen. These measurements were characterised by a plateau structure with the low FIP elements forming the first plateau, the middle FIP elements being the transition part, and the high FIP elements forming a second plateau where they were not enriched relative to each others.

1.2 Models

Different theoretical models have been developed in order to explain the FIP effect both in the upper solar atmosphere and in solar wind. Most of the models locate the fractionation process in the chromosphere, where the first ionisation occurs.

The first kind of model neglects the role of the magnetic field in the fractionation, or use it only to guide the ions. In this model fractionation is driven by diffusion along field lines. Models of this kind are implemented by Marsch et al. (1995), Wang (1996) and Peter (1998). Peter's model is explained in detail in chapter 4. A common feature for these diffusion models is that an enrichment can be obtained if the minor constituent velocity at the bottom of the studied layer exceeds the velocity of the hydrogen background (see eq.4.10).

A second kind of model describes the magnetic field as the key element in the fractionation process. At low enough densities, (such that neutral and ionised atoms are not coupled) high FIP elements (that are still neutral) can move perpendicularly to the field lines, whereas this is not possible for low FIP elements that at these chromospheric heights are already ionised. The fractionation thus derives from a difference in the drift velocities between high and low FIP elements. This velocity difference becomes significant when the collision frequency between ionised and neutral atoms can be neglected relative to the gyro frequency. Under this condition the neutral species (high FIP) can cross the field lines while the ionised species are forced to follow the field. An example for this kind of models is given by Vauclair (1996) where an ascending horizontal magnetic field lift the ionised elements, whereas the neutral cross the field lines because of gravity, leading to an enrichment of low FIP element in the upper part of the atmosphere. Other models of this kind are presented by von Steiger and Geiss (1989) and Henoux and Somov (1997).

1.3 The present work

There is still no wide agreement upon the processes behind the FIP effect and both more observation and more theoretical models are needed to obtain a clearer picture of the fractionation process.

In this work we will focus on the fractionation process in fast solar wind.

Building a one dimensional numerical model of the chromosphere we will try to understand the ionisation-separation process that is believed to be behind fractionation. First we will implement a model describing the hydrogen background in a chromospheric layer, with a flow corresponding to the solar wind flux obtained by measurements. Three different supposed geometry will give three different characteristic velocities for the model. Then we will build a similar model describing the interaction between some minor constituents (oxygen, neon, magnesium, silicon and iron) and the hydrogen background in order to study how and if fractionation can take place, with different background fluxes. The result will be compared with the work by Peter (1998) and Peter and Marsch (1998), discussing their ad-hoc chosen boundary conditions and parameters and how these influence the possibility to obtain a FIP effect comparable with measurements.

Chapter 2

The model

We consider a slab of the solar atmosphere of a certain thickness and with a certain temperature profile. For simplicity we consider the atmosphere as a one dimensional system with plane parallel symmetry.

The atmosphere model consists of a pure hydrogen background (see section 5) and one of the trace elements (minor constituents) O, Ne, Mg, Si or Fe at the time. Only neutrals and singly ionised particles are included, and the hydrogen background is quasi neutral, i.e. the electron density is the same as the proton density.

The physical quantities are governed by the mass conservation (mass continuity equation) and the momentum equation (Newton's second law). No energy equation is solved, but a linear temperature profile is given. In this way we avoid the problems related to the coupling between the radiative transport equation and the hydrodynamic equations.

We consider a magnetic field with vertical magnetic flux lines and flow, in vertical direction only. Hence, since the contribution from the magnetic field is proportional to the vector product between the magnetic field and the velocity, we do not need to include any magnetic field term in the momentum equation.

We model the following equations

$$\frac{\partial n_i}{\partial t} + \frac{\partial}{\partial z}(n_i\ u_i) = n_j\ P_{ji} - n_i\ P_{ij} \tag{2.1}$$

$$\begin{aligned}\frac{\partial (n_i u_i)}{\partial t} + \frac{\partial}{\partial z}(n_i u_i u_i) = &- \frac{1}{m_i}\frac{\partial}{\partial z}(n_i k T) + g n_i + n_j u_j\ P_{ji} - n_i u_i P_{ij} \\ &+ \frac{n_i q_i}{m_i}\ E + \sum_{j \neq i} n_i \nu_{ij}(u_j - u_i)\end{aligned} \tag{2.2}$$

where the indexes i and j can take the values 1 or 2, representing neutral gas and ionised gas, respectively. n_i is the number density and u_i is the velocity of the species i. P_{12} is the ionisation rate and P_{21} the recombination rate, both discussed in section 2.1. m_i and q_i are the mass and the electric charge of the species i, respectively. E is the electric field (see section 2.4) and ν_{ij} is the collision frequency between the species i and j. The collision frequencies are treated in section 2.5. g is the gravitational acceleration, set to $g = -270$ m s^{-2}, T is the temperature (constant in time) and k is Boltzmann's constant. The derivatives in equation 2.1 and 2.2 are taken with respect to time t and height z. All the variables are in SI-units, if nothing else is specified.

We model the background with the same equations (2.1 and 2.2) as for the minor constituents, but for practical reasons we rewrite the momentum equation for neutral hydrogen and protons as

$$\frac{\partial(n_H u_H)}{\partial t} + \frac{\partial}{\partial z}(n_H u_H u_H) = -\frac{1}{m_H}\frac{\partial}{\partial z}(n_H kT) + g n_H + k_{mt}\ n_H\ n_p(u_p - u_H) + n_p u_p\ P_{21} - n_H u_H P_{12} \tag{2.3}$$

$$\frac{\partial(n_p u_p)}{\partial t} + \frac{\partial}{\partial z}(n_p u_p u_p) = -\frac{2}{m_p}\frac{\partial}{\partial z}(n_p kT) + g n_p + k_{mt}\ n_p\ n_H(u_H - u_p) + n_H u_H\ P_{12} - n_p u_p P_{21}\ . \tag{2.4}$$

The collisions between protons and neutral hydrogen are dominated by the charge transfer process, and due to Newton's third law, their collision rate coefficients k_{mt} are equal. This rate coefficient depends on the temperature, and we have adopted the following relation between k_{mt} and T,

$$k_{mt} = k_{mt}(T) = 1 \times 10^{-14}\sqrt{\frac{T_H + T_p}{10^4\ \mathrm{K}}}\ , \tag{2.5}$$

in units m^3 s^{-1}, where the neutral hydrogen and proton temperatures, T_H and T_p, are both equal the electron temperature T. In order to check if this is a reasonable estimation of the collision frequency we have compared it with the values of the rate coefficient k_{mt} provided by Schultz et al. (2008). They give two values of k_{mt} in our temperature range, $k_{mt} = 1.59 \times 10^{-14}$ m^3 s^{-1} at $T = 7 \times 10^3$K and $k_{mt} = 1.82 \times 10^{-14}$ m^3 s^{-1} at $T = 1 \times 10^4$K. These values are higher than what equation 2.5 yields at the same temperatures, i.e. $k_{mt}(T = 7{\times}10^3\mathrm{K}) = 1.19{\times}10^{-14}$ m^3 s^{-1} and $k_{mt}(T = 1{\times}10^4\mathrm{K}) = 1.41{\times}10^{-14}$ m^3 s^{-1}, but they agree within an uncertainty of 30%. The factor two in the pressure term for protons is due to the electric field, described in section 2.4.

2.1 Ionisation rates

The ionisation rate P_{ij} can be written as the sum of the radiative ionisation R_{ij} and the collisional ionisation C_{ij},

$$P_{ij} = R_{ij} + C_{ij} \ . \tag{2.6}$$

For the hydrogen background, the collisional ionisation rate is almost always negligible. For oxygen we also take charge transfer with hydrogen into account (see section 2.3). The collisional and radiative ionisation rates for oxygen are negligible.

2.1.1 Radiative Ionisation

Hydrogen For the radiative ionisation we follow the approach of Peter and Marsch (1998). In that model the ionising radiation is assumed to come from above. In other words the photons that have the right energy to ionise hydrogen are assumed to come from the upper layers of the solar atmosphere. Supposing a constant photon flux at the top of our layer, the ionising radiation flux and the photoionisation rate R_{12} vary with depth in the atmosphere. Assuming a photoionisation cross section σ_H that is constant for the relevant wavelength band we can write:

$$\frac{d}{ds}R_{12} = -\sigma_H R_{12} n_H, \tag{2.7}$$

where $s = z_{top} - z$ is the depth, z the height, z_{top} the height of the layer's upper boundary and n_H is the neutral hydrogen density. The photoionisation cross section for hydrogen can be estimated as $\sigma_H = 5.5 \times 10^{-22}$ m^2 (Peter and Marsch, 1998) (Vernazza et al., 1981). Solving equation 2.7, with a change of variable from s to z we get:

$$R_{12}(z) = R_{12}\left(z_{top}\right) \exp\left(-\sigma_H \int_z^{z_{top}} n_H(z')dz'\right). \tag{2.8}$$

If the neutral hydrogen density is known the rate can be estimated by numerical integration.

By supposing an initial value for $R_{12}(z)$ we can integrate the fluid equations until we obtain a steady state. With n_H we can calculate a new value for R_{12} from equation 2.8. We continue the iteration until R_{12} changes by less than 3% from one iteration to the next.

Minor constituents For the radiative ionisation of the minor constituents we follow the approach of Peter (1998). As for hydrogen the ionising radiation is assumed to come from above, that gives a decaying ionisation rate.

	$R_{ni}[\mathrm{s}^{-1}]$
O	1.62×10^{-2}
Ne	1.24×10^{-2}
Si	9.23×10^{-1}
Mg	1.28
Fe	1.099

Table 2.1: *Ionisation rates.*

However the minor constituents are characterised by a low abundance. This gives a negligible absorption of the ionising radiation. The ionisation rate can thus be considered constant throughout the slab.

The photoionisation rates for zero optical depth are given in table 2.1 and are taken from von Steiger and Geiss (1989) and Peter (1998).

2.1.2 Collisional ionisation

There are several different ionisation mechanisms due to collisions. We only consider *direct ionisation* in this work. Direct ionisation happens when an atom collides with an electron producing two electrons and a singly ionised atom. The direct ionisation rates for the elements H, O, Ne, Mg and Si are taken from Arnaud and Rothenflug (1985), while the direct ionisation rate for iron is taken from Arnaud and Raymond (1992). The rate coefficient for direct ionisation can be written

$$c_{DI}(T) = 6.69 \cdot 10^{-13} \ \left(\frac{e}{kT}\right)^{3/2} \ \frac{\exp(-x)}{x} F(x) \ , \tag{2.9}$$

in units of $\mathrm{m}^3\ \mathrm{s}^{-1}$, where

$$x = \frac{eI}{kT} \tag{2.10}$$

$$\begin{aligned} F(x) =& A \ (1 - x \ f_1(x)) \ + B \ (1 + x - x(2+x) f_1(x)) \\ &+ C \ f_1(x) + D \ x \ f_2(x) \end{aligned} \tag{2.11}$$

$$f_1(x) = e^x \int_1^\infty \frac{dt}{t} e^{-tx} \tag{2.12}$$

$$f_2(x) = e^x \int_1^\infty \frac{dt}{t} e^{-tx} \ \ln(t) \ . \tag{2.13}$$

I is the first ionisation potential in units V, e is the elementary charge and A, B, C and D are fitting coefficients given in table 2.2. The integral $f_1(x)$

is evaluated using the *Hastings polynomial approximation*

$$x\ f_1(x) = x\ e^x \int_1^\infty \frac{dt}{t} e^{-tx} = \frac{x^4 + a_1 x^3 + a_2 x^2 + a_3 x + a_4}{x^4 + b_1 x^3 + b_2 x^2 + b_3 x + b_4} + \epsilon(x)\ , \quad (2.14)$$

(Abramowitz and Stegun, 1964), where $|\epsilon(x)| < 2 \times 10^{-3}$ and

$$a_1 = 8.573328740 \quad b_1 = 9.573322345 \quad (2.15)$$
$$a_2 = 18.05901697 \quad b_2 = 25.63295615 \quad (2.16)$$
$$a_3 = 8.634760893 \quad b_3 = 21.09965308 \quad (2.17)$$
$$a_4 = 0.267773734 \quad b_4 = 3.958496923\ . \quad (2.18)$$

$f_2(x)$ is evaluated following Hummer (1983), and the final ionisation rate C_{12} defined in chapter 2 is given by

$$C_{12} = c_{DI}\ n_p\ , \quad (2.19)$$

in units s^{-1}.

2.2 Recombination rates

The recombination rate P_{21} of the minor constituents can be written as the sum of the radiative recombination R_{21} and the dielectronic recombination D_{21}. The radiative recombination is a form of spontaneous emission. The dielectronic recombination is a process where an unbound electron binds to the recombining ion giving its energy to the atom by exciting one of its other electrons. The excited atom deexcitates by emitting a photon. For hydrogen we obviously only have radiative recombination.

2.2.1 Radiative recombination for hydrogen

The radiative recombination rate coefficient for hydrogen is given by

$$\alpha_r(T) = 5.197 \times 10^{-20}\ \lambda^{1/2}\ \left(0.4288 + 0.5\ \ln(\lambda) + 0.469\ \lambda^{-1/3}\ \right)\ , \quad (2.20)$$

(Arnaud and Rothenflug, 1985), in units $\mathrm{m}^3\ \mathrm{s}^{-1}$, where $\lambda = 157890/T$ and T is given in K. In order to get the rate R_{ij} measured in s^{-1}, as defined in chapter 2, $\alpha_r(T)$ has to be multiplied by the electron number density, which in our model is the same as the proton number density,

$$P_{21} = R_{21} = \alpha_r\ n_p. \quad (2.21)$$

2.2.2 Recombination rates for the minor constituents

The equation for the radiative recombination rate coefficient in units $\mathrm{m}^3\ \mathrm{s}^{-1}$ (Shull and van Steenberg, 1982) is the same for all the minor constituents,

$$\alpha_r(T) = A_{rad}\ \left(\frac{T}{10^4\mathrm{K}}\right)^{X_{rad}} \quad . \tag{2.22}$$

The fitting coefficients, A_{rad} and X_{rad}, are given in table 2.3. Also the dielectronic recombination rate coefficient, in units $\mathrm{m}^3\ \mathrm{s}^{-1}$ (Shull and van Steenberg, 1982), is the same for O, Ne, Mg and Si,

$$\alpha_d(T) = A_{di}\ T^{-\frac{3}{2}}\ \exp\left(-\frac{T_0}{T}\right)\ \left(1 + B_{di}\ \exp\left(-\frac{T_1}{T}\right)\right)\ . \tag{2.23}$$

The fitting coefficients A_{di}, B_{di}, T_0 and T_1 are given in table 2.3. As for hydrogen, these rate coefficients have to be multiplied with the electron (proton) density in order to get the recombination rate P_{21} in units of s^{-1},

$$P_{21} = R_{21} + D_{21} = (\alpha_r + \alpha_d)\ n_p. \tag{2.24}$$

2.2.3 Dielectronic recombination rate for iron

The equation for the dielectronic recombination rate for iron is given by

$$\alpha_d(T) = T^{-\frac{3}{2}}\ \sum_j c_j\ \exp\left(-\frac{E_j\ e}{kT}\right)\ , \tag{2.25}$$

in units $\mathrm{m}^3\ \mathrm{s}^{-1}$ (Arnaud and Raymond, 1992). E_j and c_j are given by

$$E_1 = 5.12\ \mathrm{eV} \quad c_1 = 2.2 \times 10^{-10}\ \mathrm{m}^3\ \mathrm{s}^{-1}\ \mathrm{K}^{3/2} \tag{2.26}$$

$$E_2 = 12.9\ \mathrm{eV} \quad c_2 = 1.0 \times 10^{-10}\ \mathrm{m}^3\ \mathrm{s}^{-1}\ \mathrm{K}^{3/2}\ . \tag{2.27}$$

2.3 Charge transfer

The charge transfer ionisation and charge transfer recombination are, in a first approximation, the predominant transition processes for oxygen. In the charge transfer ionisation an electron jumps from a neutral oxygen to a proton resulting in a ionised oxygen and neutral hydrogen atom. Vice versa, in charge transfer recombination, an ionised oxygen and a neutral hydrogen meet to form neutral oxygen and a proton. Treating this process as a normal

Element	I	A	B	C	D
O	13.6	9.5	-17.5	12.5	-19.5
Ne	21.6	40.0	-42.0	18.0	-56.0
Mg	7.6	18.0	-1.0	0.6	-4.0
Si	8.1	74.5	-49.4	1.3	-54.6
Fe	7.9	31.9	-15.0	0.32	-28.1

Table 2.2: Fitting coefficients for the direct ionisation rates.

	A_{rad} (m^3 s^{-1})	X_{rad}	A_{di} (m^3 s^{-1} $K^{3/2}$)	B_{di}	T_0 (K)	T_1 (K)
O	3.10(-19)	6.78(-1)	1.11(-9)	9.25(-2)	1.75(5)	1.45(5)
Ne	2.20(-19)	7.59(-1)	9.77(-10)	7.30(-2)	3.11(5)	2.06(5)
Mg	1.40(-19)	8.55(-1)	4.49(-10)	2.10(-2)	5.01(4)	2.81(4)
Si	5.90(-19)	6.01(-1)	1.10(-9)	0.0	7.7(4)	0.0
Fe	1.42(-19)	8.91(-1)	-	-	-	-

Table 2.3: Fitting coefficients for the recombination rates. $3.10(-19)$ means 3.10×10^{-19}.

transition between neutral and ionised oxygen the transition rates are given by

$$P_{12} = n_p \, C_{ION} \tag{2.28}$$
$$P_{21} = n_H \, C_{REC} \tag{2.29}$$

in units s^{-1}, where n_p and n_H is the proton and the neutral hydrogen number density, respectively. The rate coefficients C_{ION} and C_{REC} are given by

$$C_{ION} = 0.91 \times 10^{-15} \, \exp\left(\frac{-19.6 \times 10^{-3} \text{ V}}{kT} e\right) \left(1 - 0.93 \, \exp\left(-\frac{T}{10^3 \text{K}}\right)\right) \tag{2.30}$$

$$C_{REC} = 10^{-15} \, \left(1 - 0.66 \, \exp\left(-9.3 \frac{T}{10^4 \text{K}}\right)\right) \, , \tag{2.31}$$

in units m^3 s^{-1} (Arnaud and Rothenflug, 1985).

2.4 Electric field

To obtain a simple expression for the electric field we write the momentum equation for the electrons,

$$\frac{\partial(n_e u_e)}{\partial t} + \frac{\partial}{\partial z}(n_e u_e u_e) = -\frac{1}{m_e}\frac{\partial}{\partial z}(n_e kT) + g n_e - \frac{n_e e}{m_e} E \ , \tag{2.32}$$

where m_e is the electron mass, n_e is the electron number density, u_e is the velocity of the electrons. Since the electron mass m_e is much smaller than every other variable, we can neglect all the terms that are not divided by m_e, and equation 2.32 becomes

$$-\frac{\partial}{\partial z}(n_e kT) = n_e \ e \ E \ . \tag{2.33}$$

We have assumed that the sun's atmosphere is quasi neutral, and hence $n_e = n_p$. Substituting this in equation 2.33 we obtain

$$-\frac{\partial}{\partial z}(n_p kT) = n_p \ e \ E \ , \tag{2.34}$$

which yields the following expression for the electric field,

$$E = -\frac{1}{e \ n_p}\frac{\partial}{\partial z}(n_p kT) \ . \tag{2.35}$$

2.5 Collisions

The collision processes describe how the minor constituents interact with the hydrogen background. In this section we will treat three different collision processes. Neutral-neutral collisions (collisions between neutral minor constituents and neutral hydrogen), neutral-ion collisions (both collisions between neutral minor constituents and protons, and collisions between neutral hydrogen and ionised minor constituents), and finally the very important collisions between ionised particles (protons and ionised minor constituents). Collisions between two minor constituents are neglected.

Proton-ion collisions are the absolutely strongest ones. Their rate coefficients are at least two (often three) orders of magnitude stronger than the rate coefficients for neutral-ion and neutral-neutral collisions. Neutral-neutral and neutral-ion collisions have rate coefficients of the same order of magnitude.

Element	$r_{nH}(10^{-10}\mathrm{m})$
Oxygen	2.26
Neon	1.75
Silicon	2.91
Magnesium	3.09
Iron	3.09

Table 2.4: Atomic radius for the rigid sphere approximation, taken from Marsch et al. (1995).

2.5.1 Neutral-neutral collisions

When describing the collisions between neutral particles we use the so called *rigid sphere approximation*. The collision frequency for neutral-neutral collisions (Banks and Kockarts, 1973) (Schunk, 1977) is given by

$$\nu_{12} = \frac{4}{3}\frac{m_2}{m_1 + m_2}\, n_2\, \sigma_0\, v_{12}\ , \tag{2.36}$$

in units s^{-1}, where m_1 and m_2 are the masses of the colliding particles, v_{12} is the relative velocity, n_2 is the number density of the neutral hydrogen gas, and $\sigma_0 = \pi r_{nH}^2$ is the collision cross section. The values of r_{nH} for the different minor constituents (Marsch et al., 1995) are given in table 2.4. Assuming thermal and dynamic equilibrium, the distribution of the velocities is given by the Maxwell distribution and the average relative speed between the particles is

$$v_{12} = \left(\frac{8\ k}{\pi}\ \frac{T}{\mu}\right)^{\frac{1}{2}}\ , \tag{2.37}$$

where the reduced mass μ is given by

$$\mu = \frac{m_1\ m_2}{m_1 + m_2}. \tag{2.38}$$

Equation 2.36 and 2.37 yields the following expression for the collision frequency,

$$\nu_{12} = \frac{4}{3}\ \frac{m_2}{m_1 + m_2}\ n_2\ \sigma_0 \left(\frac{8\ k}{\pi}\ \frac{T}{\mu}\right)^{\frac{1}{2}}. \tag{2.39}$$

2.5.2 Neutral-ion collisions

In a neutral-ion collision the most important interaction is represented by an induced dipole attraction. The average collision rate (Schunk, 1977), in

Element	α
Hydrogen	0.74
Oxygen	0.88
Iron	9.3
Neon	0.44
Silicon	6.0
Magnesium	11.8

Table 2.5: Neutral gas atomic polarizability. $[\alpha] = 10^{-40}$ C^2 s^2 kg^{-1}

units s^{-1}, is given by

$$\nu_{12} = \frac{4}{3} \frac{m_2}{m_1 + m_2} n_2 \, v_{12} \, Q_D. \tag{2.40}$$

n_2 is now or the neutral or the ionised hydrogen number density, and Q_D is the average momentum transfer cross section for collisions between ions and neutral particles, given by

$$Q_D = 0.260 \left(\frac{\alpha}{kT} \right)^{\frac{1}{2}} \frac{e}{\epsilon_0} \, , \tag{2.41}$$

where α is the neutral gas atomic polarizability and ϵ_0 is the permittivity of vacuum. The polarizabilities α for the different elements (Marsch et al., 1995) are given in table 2.5. The average relative speed is given by the same formula as for collisions between neutral particles (see equation 2.37), and with the expression for the cross section in equation 2.41, equation 2.40 can be written as

$$\nu_{12} = 0.553 \frac{m_2}{m_1 + m_2} n_2 \left(\frac{\alpha}{\mu} \right)^{\frac{1}{2}} \frac{e}{\epsilon_0}. \tag{2.42}$$

2.5.3 Ion-ion collisions

Collisions between charged particles are described by the so called *Coulomb interaction*. The collision frequency for such collisions (Schunk, 1977), in units s^{-1}, is given by

$$\nu_{12} = \frac{1}{3 \, \epsilon_0^2} \frac{n_2 \, m_2}{m_1 + m_2} \left(\frac{2\pi kT}{\mu_{12}} \right)^{-\frac{3}{2}} \frac{e_1^2 \, e_2^2}{\mu_{12}^2} \ln \Lambda \, , \tag{2.43}$$

where the electric charge e_1 and e_2 of the two particles are, in our case, both equal the elementary charge e. This is because we only treat singly ionised

ions. The *Coulomb logarithm*, $\ln \Lambda$, is given by

$$\Lambda = 24\pi \; n_e \; L_D^3 \; , \tag{2.44}$$

where L_D is the Debye length, that for a pure hydrogen plasma is given by

$$L_D = \left(\frac{4\pi}{kT} \; \frac{e^2}{4\pi\epsilon_0} \; (n_e + n_p) \right)^{-\frac{1}{2}} \; . \tag{2.45}$$

Since we study a quasi neutral atmosphere, i.e. $n_e = n_p$, equation 2.45 may be written as

$$L_D = \sqrt{\frac{kT\epsilon_0}{2e^2 n_p}} \; . \tag{2.46}$$

Finally we obtain the following expression for the Coulomb logarithm,

$$\ln \Lambda = \ln \left(\frac{24\pi n_p}{e^3} \left(\frac{kT\epsilon_0}{2n_p} \right)^{\frac{3}{2}} \right) . \tag{2.47}$$

Chapter 3

The numerical model

3.1 Double grid

The model describes a slab of the solar atmosphere of a given thickness. The slab is divided into cells, where every cell is characterised by a lower border, an upper border and a centre. Some physical quantities are defined in the cell's centre while others are defined on the cell's borders. This is why the system is called a "double grid": the cells' borders constitute a first grid, *the border grid*, and the cells' centres define a second grid, *the centre grid*. The gas velocity and the mass flux are defined on the border grid, while the gas densities and the gas temperature are defined on the centre grid.

Going into details, we define a velocity u_j that describes the gas velocity on the j-th border and a density n_j that gives the gas density in the centre of the j-th cell, where j is the spatial discretisation index. As one can see from Fig. 3.1 the j-th cell is delimited between the borders labelled as j and $j+1$. Then the j-th border is the limit between the j-th and the $j-1$-th cell.

Like the velocity, the mass flux, given by $n\ u$, is also calculated on the border and we therefore need an estimate of the density on the border, called $\hat{n}_j$. In the code, two different ways to estimate the density values on the

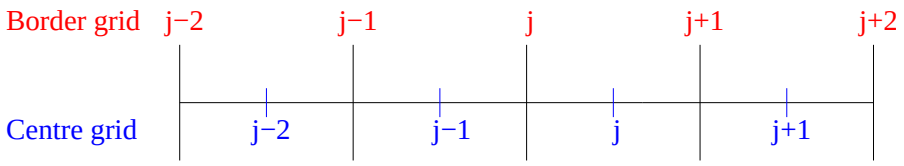

Figure 3.1: The double grid structure.

borders have been used. The first one is an easy two points average,

$$\hat{n}_j = \frac{1}{2}(n_{j-1} + n_j), \tag{3.1}$$

and the second one is a more elaborated average using a second order upwind differencing scheme to estimate an advective flux. The two points average is used in all terms of equation 2.2, except the first term on the right hand side (pressure gradient term), which has no need for any value of $\hat{n}_j$, and the second term on the left hand side (advection term), where the upwind scheme is used. The latter is also used in the second term of the left hand side of equation 2.1.

In the same way, we can define the averaged velocity of the cell centre,

$$\hat{u}_j = \frac{1}{2}(u_j + u_{j+1}), \tag{3.2}$$

but this time only the two points average has been used.

3.2 Semi-implicit scheme

The aim of the code is to integrate the continuity and the momentum equations (equation 2.1 and 2.2) in time. The scheme used to solve these equations is a semi-implicit scheme, which means that it is a mix of an explicit and an implicit scheme.

In the explicit part every unknown variable is a function of known variables only. To exemplify we consider the quantity $q(p, r)$, which is a function of the quantities p and r. In an explicit scheme at a certain time step $i + 1$, the quantity q is only a function of p and r at previous time steps, $q^{i+1} = q^{i+1}(p^i, r^i, p^{i-1}, ...)$. The explicit scheme for the left hand side of the continuity equation is given by

$$\frac{n_j^{i+1} - n_j^i}{\Delta t} + \frac{\left(\hat{n}_{j+1}^i \; u_{j+1}^i - \hat{n}_j^i \; u_j^i\right)}{\Delta z} \; . \tag{3.3}$$

Thus, the explicit scheme provides an easy way to determine numerically the evolution of the physical quantities when the values at the previous time step are known. Unfortunately, explicit methods are characterised by unstable solutions. These can be studied introducing the Courant-Friedrichs-Lewy stability criterion (Press et al., 1992), which sets a lower limit for the ratio between spatial increment Δz and time step Δt.

The code is used to find both time dependent and steady state solutions, which requires big time steps. It is therefore preferable to avoid any upper

limit for the time step Δt. In order to avoid this, we need to use an implicit scheme.

In implicit schemes, the quantity q^{i+1} is coupled with all the other quantities at the same time step, $q^{i+1} = q(p^{i+1}, r^{i+1}, p^i, r^i, ...)$. It is therefore no longer possible to calculate explicitly every quantity one by one. Hence, the whole system of coupled equations needs to be solved for each time step t_i. The implicit scheme for the left hand side of the continuity equation becomes

$$\frac{n_j^{i+1} - n_j^i}{\Delta t} + \frac{\left(\hat{n}_{j+1}^{i+1}\ u_{j+1}^{i+1} - \hat{n}_j^{i+1}\ u_j^{i+1}\right)}{\Delta z}\ . \tag{3.4}$$

Since all the quantities are coupled in the implicit scheme, there is no upper limit for time step Δt. In our code implicit and explicit parts are mixed, i.e. the variables in the advective term of the continuity equation (2.1) and the momentum equation (2.2) are defined as

$$\bar{u}_j = \beta\ u_j^{i+1} + (1-\beta)\ u_j^i \tag{3.5}$$

and

$$\bar{\hat{n}}_j = \beta\ \hat{n}_j^{i+1} + (1-\beta)\ \hat{n}_j^i, \tag{3.6}$$

where β determines how implicit the code is. $\beta = 0$ gives a fully explicit code, $\beta = 1$ gives a fully implicit code, and any number between 0 and 1 makes the code semi-implicit.

By defining the cell volume $\Delta V = A\Delta z$, where A is the unit surface, equation 3.3 can be written as

$$\Delta V\left(n_j^{i+1} - n_j^i\right) + A\Delta t\left(\bar{\hat{n}}_{j+1}\ \bar{u}_{j+1} - \bar{\hat{n}}_j\ \bar{u}_j\right) = 0. \tag{3.7}$$

The discretisation of the right hand side of the continuity equation (equation 2.1) proceeds similarly, with the only note that we choose to write the ionisation term as a fully implicit - and not semi-implicit - term.

Also the discretisation of the momentum equation follows the same steps, and the explicit expression for the left hand side of equation 2.2 is,

$$\begin{aligned}&\frac{\hat{n}_j^{i+1}u_j^{i+1} - \hat{n}_j^i u_j^i}{\Delta t} + \\ &\frac{\left(\hat{n}_{j+1}^i u_{j+1}^i + \hat{n}_j^i u_j^i\right)\hat{u}_j^i - \left(\hat{n}_j^i u_j^i + \hat{n}_{j-1}^i u_{j-1}^i\right)\hat{u}_{j-1}^i}{\Delta z}\ .\end{aligned} \tag{3.8}$$

A combination of equation 3.8 and the corresponding implicit scheme gives the semi-implicit expression

$$\begin{aligned}\Delta V\left(\hat{n}_j^{i+1}u_j^{i+1} - \hat{n}_j^i u_j^i\right) + A\Delta t\left(\bar{\hat{n}}_{j+1}\bar{u}_{j+1} + \bar{\hat{n}}_j\bar{u}_j\right)\bar{\hat{u}}_j \\ - \left(\bar{\hat{n}}_j\bar{u}_j + \bar{\hat{n}}_{j-1}\bar{u}_{j-1}\right)\bar{\hat{u}}_{j-1}\ ,\end{aligned} \tag{3.9}$$

where we have defined

$$\bar{\hat{u}}_j = \beta\ \bar{u}_j^{i+1} + (1-\beta)\ \bar{u}_j^i\ . \tag{3.10}$$

Without going into details, we will describe how the different terms on the right hand side of the momentum equation (2.2) can be implemented in a discretised scheme, by specifying if the implicit or semi-implicit form is used. The *pressure gradient* term contains semi-implicit centre-grid values of the density, defined similarly to equation 3.6. The *electric field* term is equal to the pressure gradient term in the hydrogen background, which means that it contains semi-implicit centre-grid values of the (proton) density. In the code for the minor constituents the electric field depends on the fully implicit minor constituent density value at the cell borders, and on the time-independent proton pressure also evaluated at the cell borders. The *gravity* term depends on the semi-implicit border-grid values of the density. The *ionisation*, the *charge transfer* and the *collision* terms are calculated from fully implicit border-grid values of the density and the velocity.

3.3 Newton-Raphson method

As we have seen in section 3.2, a semi-implicit scheme leads to a system of coupled nonlinear equations that we want to solve with respect to n^{i+1} and u^{i+1} for every time step i. In order to do this, the Newton-Raphson method is applied (Press et al., 1992). As a first step, we define a vector E_j that contains all the discretised system equations, both for the continuity and for the momentum equation. These equations have a component for every cell j.

The solution for the $i+1$ time step yields the value n^{i+1} and u^{i+1} for which

$$E_j(n_k^{i+1}, u_k^{i+1}, n_{k-1}^{i+1}, \ldots) = E_j(x_k^{i+1}, \ldots) = 0, \tag{3.11}$$

where x_k^i is a vector of components n_k^i, u_k^i, and k is a second space index. We write x_k^{i+1} as the sum of the previous value x_k^i and a correction Δx_k^i,

$$x_k^{i+1} = x_k^i + \Delta x_k^i, \tag{3.12}$$

where Δx_k^i is the unknown variable. If the time step is small enough, we assume that also the corrections are small,

$$\frac{|\Delta x_k^i|}{x_k^i} \ll 1. \tag{3.13}$$

With this assumption it is possible to linearise the solution, neglecting the higher order terms in $\frac{|\Delta x|}{x}$, e.g.,

$$x_k^{i+1} \cdot x_k^{i+1} \approx x_k^i \cdot x_k^i + 2x_k^i \Delta x_k^i + \text{higher orders.} \tag{3.14}$$

Let us assume that we do not know the real solutions x_k^{i+1}, but only their estimate x_k^t, called test solution. Then the vector $\underline{E}$ is no longer zero, but quantifies the error from the estimate. The aim of the Newton-Raphson method is to find the right correction that nullifies the error, or at least makes it negligible. The steps of the Newton-Raphson method are given by

$$E_j(x_k^t) \neq 0, \tag{3.15}$$

$$E_j(x_k^t + \Delta x_k) = 0. \tag{3.16}$$

Assuming again that the correction is small, $\frac{|\Delta x_k|}{x_k^t} \ll 1$, we can rewrite E_j as a Taylor series

$$E_j(x_k^t + \Delta x_k) \approx E_j(x_k^t) + \sum_k \frac{\partial E_j}{\partial x_k}\Big|_{x_k = x_k^t} \Delta x_k = 0. \tag{3.17}$$

By defining a new operator W_{jk} as

$$W_{jk} = -\frac{\partial E_j}{\partial x_k}, \tag{3.18}$$

we can rewrite equation 3.17 as

$$E_j(x_k^t + \Delta x_k) \approx E_j(x_k^t) - \sum_i W_{jk}(x_k^t)\Delta x_k = 0, \tag{3.19}$$

or in matrix form

$$\mathbf{W} \cdot \underline{\Delta x} = \underline{E}(\underline{x}^t). \tag{3.20}$$

If we invert the matrix W, we get

$$\Delta \underline{x} = \mathbf{W}^{-1} \underline{E}(\underline{x}^t), \tag{3.21}$$

that allows us to calculate a new value of $\underline{x}$,

$$\underline{x}^{t'} = \underline{x}^t + \Delta \underline{x}. \tag{3.22}$$

The partial derivatives that constitute the matrix element W_{jk} are different from zero only when $j - 2 \leq k \leq j + 2$, because of the second order

upwind scheme used in the advective term. This results in a pentadiagonal matrix, with big simplifications concerning the matrix inversion.

The Newton-Raphson method gives exact result when the system is made up of linear equations. This is not the case here, because in the Taylor expansion we have neglected all the higher order terms including the second order. However, if the test solution is not too far from the real solution, i.e. $\frac{|\Delta x|}{x} \ll 1$, hopefully the new solution obtained with the Newton-Raphson method can bring us closer to the right solution. If this is the case, we can solve the system with an iterative procedure, otherwise, if the new solution is not converging, it is necessary to repeat the whole process with a smaller time step Δt.

3.4 Boundary conditions

In this section we will describe the role of the boundary conditions, and how they are implemented. The physical values of the boundary conditions are not the same for the background and the minor constituents, and also vary between the different background models. They are therefore given for each specific case in later sections.

The boundary conditions are very important because they describe the physical system outside the grid and constitute the way to communicate all the necessary external conditions to the modelled layer. For example it is through the boundary conditions that we simulate the presence of the atmosphere below the lower boundary, avoiding in this way the whole atmosphere to fall in a gravitational collapse.

The boundary conditions supply the values for the border density $\hat{n}$ (see section 3.1) and the border velocity u on the left border of the first cell and on the last cell's right border.

It is important to differentiate the *fixed* and the *floating* boundary conditions. While a fixed boundary forces the boundary to have a determined value, the floating condition allows the boundary to just follow the same behaviour as the nearby grid points. A typical example of a floating boundary equation is the flux conservation, where the particle flux is conserved from the first grid point to the second.

Specifying a fixed density value simulates a rigid wall at the beginning or end of the grid, and can often cause reflection problems. In order to give information about the physical system without building a reflective wall we use the method of characteristics described by Korevaar and van Leer (1988).

The main idea is to build a boundary condition that has a non-reflective behaviour but is still carrying information from the system outside the grid.

This is achieved by a set of equations that permits the boundary to oscillate around a fixed value, in order for the perturbations to pass through it.

Lower boundary This method considers a undisturbed hydrogen gas at the lower boundary (where $z = z_0$) which has fixed values for the density and velocity, n_o and u_o, respectively. The true boundary value n_l and u_l are calculated by a sort of interpolation between the undisturbed values n_o and u_o and the densities and velocities at the first and the second grid pointn_1, u_1, n_2 and u_2. The boundary condition for the density is then given by

$$n_l = \frac{1}{kT_0} exp\left(\frac{\gamma(a_l + u_0 - u_1) + c_0 \log(n_0 kT_0) + c_1 \log(n_1 kT_1)}{c_0 + c_1}\right) \tag{3.23}$$

where $c_o = \sqrt{\frac{kT_0}{m_H}}$ is the sound speed of a pure hydrogen gas at temperature T_0, and m_H is the hydrogen mass. γ is the heat capacity ratio, and the parameter a_l is given by

$$a_l = \frac{z_1 - z_0}{z_2 - z_1}\left[\frac{c_2}{\gamma}\log\left(\frac{n_1 T_1}{n_2 T_2}\right) - (u_1 - u_2)\right]. \tag{3.24}$$

where c_i, T_i, and z_i are the sound speed, the temperature and the height for the first ($i = 1$) and the second ($i = 2$) grid point. The boundary condition for the velocity is given by

$$u_l = u_0 - \frac{c_0}{\gamma}\log\left(\frac{n_l}{n_0}\right). \tag{3.25}$$

Upper boundary The conditions for the upper boundary follow the same principles as for the lower boundary. The undisturbed values n_0, u_0 and n_{TOP}, u_{TOP} are specified in the different cases presented later.

Chapter 4

The ionisation-diffusion model of Peter

We are now describing the model by Peter (1998).

Since we have such a different behaviour between high and low FIP elements (see Fig. 1.2), the basic separation process is believed to happen in the chromosphere, at altitudes where elements can be found in both ionised and neutral state.

The fractionation is caused by two distinct processes: ionisation and diffusion. Elements with low FIP are characterised by a small ionisation time and they therefore couple early with the main flux of solar wind, because of the very effective Coulomb collisions with protons. Yet high FIP elements need longer time to ionise and are later coupled with hydrogen in solar wind. Thus low FIP elements are easier transported out of the chromosphere.

The other important process is diffusion. At the bottom of the ionisation layer different velocities for different elements are possible (no coupling) and these different velocities cause different abundances.

There is also a third effect that influences the fractionation, that is the velocity dependence. If the main stream of hydrogen has a high velocity, the time needed to pass through the ionisation layer is smaller and the fractionation process is less effective. If instead the wind speed is lower, the ionisation-diffusion process has more time and higher fractionation is reached.

Starting from the fluid equations, it is possible to obtain a simple formula that describes fractionation. We write the continuity equation (eq.2.1) and the momentum equation (eq.2.2) for the neutral state of a generic minor constituent x, while we assume a constant background of hydrogen. The following assumptions and approximations are used: steady state (all the time derivatives are zero), subsonic velocity (the advective term of the momentum equation can be neglected), thin slab (negligible gravity and constant

temperature), negligible electric field, homogeneous vertical magnetic field, negligible ionisation term with respect to collisions in the momentum equation, only collisions between the x minor constituent and hydrogen to be considered, and plane parallel approximation (all the variables depends only on the vertical coordinate z).

The indexes n and i correspond to the neutral and the ionised state of x, H and p refer to neutral and ionised hydrogen. By introducing the particle flux for neutral x, $\phi_n = u_n n_n$, we can rewrite the neutral continuity equation as:

$$\frac{\partial}{\partial z}\phi_n = P_{in} n_i - P_{ni} n_n, \tag{4.1}$$

while the related momentum equation becomes:

$$\frac{1}{n_n}\frac{kT}{m_x}\frac{\partial}{\partial z} n_n = \nu_{nH}(u_H - u_n) + \nu_{np}(u_p - u_n). \tag{4.2}$$

For a detailed description of all the terms and variables see chapter 2.

Summing the neutral and the ionised continuity equation we obtain that the total flux, $\Phi_x = \phi_n + \phi_i$, is constant throughout the ionisation-diffusion layer.

We now make the assumption that all the gases (minor constituents and hydrogen) are totally neutral at the bottom of the layer$(n_i^0, \phi_i^0, n_p^0, \phi_p^0 = 0)$, and furthermore, that the neutral velocity u_n is constant at the bottom, which gives:

$$\frac{\partial}{\partial z}\phi_n^0 = u_n^0 \frac{\partial}{\partial z} n_n^0. \tag{4.3}$$

We can now suppose that the collision rates are proportional with the respective (neutral or ionised) hydrogen densities, i.e. that $\nu_{nH} = \hat{\nu}_{nH} n_H$ and $\nu_{np} = \hat{\nu}_{np} n_p$, with $\hat{\nu}_{nH}$ and $\hat{\nu}_{np}$ constant.

Substituting eq. 4.1, written for the lower boundary in the left hand side of eq. 4.3, and eq. 4.2 (still written for the lower boundary) in the right hand side, we get:

$$-P_{ni} N_x^0 = u_n^0 N_x^0 \, \frac{m_x}{kT} \, \nu_{nH} \left(u_H^0 - u_n^0\right) \ , \tag{4.4}$$

where N_x^0 is the total density for the trace gas at the lower boundary. Rewriting this equation with respect to the trace gas total flux Φ_x we obtain the quadratic equation

$$\Phi_x^2 - \Phi_x \Phi_H \frac{N_x^0}{N_H} - \frac{P_{ni}}{\hat{\nu}_{nH}} \frac{kT}{m_x} \frac{(N_x^0)^2}{N_H} = 0 \ , \tag{4.5}$$

which gives the following solutions:

$$\Phi_x = \frac{\Phi_H \frac{N_x^0}{N_H} \pm \sqrt{\Phi_H^2 \left(\frac{N_x^0}{N_H}\right)^2 + 4(\omega_x N_x^0)^2}}{2} \; ; \tag{4.6}$$

where capital letters stay for total densities and total fluxes and where ω_x, called the diffusion velocity, is defined by:

$$\omega_x^2 = \frac{P_{ni}}{\hat{\nu}_{nH} N_H} \frac{kT}{m_x}. \tag{4.7}$$

By defining the average velocity $U = \Phi/N$, eq. 4.6 can be rewritten as:

$$\frac{U_x}{U_H} = 1 \pm \sqrt{1 + 4\left(\frac{\omega_x}{U_H}\right)^2}. \tag{4.8}$$

With an upstream only the plus sign leads to a physical solution. From eq. 4.8 it results that all the minor constituents have a velocity at the bottom higher than the main stream velocity.

This ratio between average velocities is closely related to the fractionation. Supposing that the key processes for fractionation take place in this ionisation-diffusion layer, the absolute fractionation (see eq. 1.1) can be rewritten as:

$$(f_{abs})_x = \frac{(\frac{N_x}{N_H})^{top}}{(\frac{N_x}{N_H})^{bottom}} \; . \tag{4.9}$$

If we now assume that at top the velocities are all coupled, $U_x = U_H$, and consider that the total fluxes are constant, the ratio N_x/N_H at the top is equal to the ratio Φ_x/Φ_H, that gives:

$$(f_{abs})_x = \frac{U_x^0}{U_H^0} \; . \tag{4.10}$$

Also the relative fractionation can be written from eq. 4.8:

$$(f_{rel})_x = \frac{U_x}{U_o} = \frac{1 + \sqrt{1 + 4\left(\frac{\omega_x}{U_H}\right)^2}}{1 + \sqrt{1 + 4\left(\frac{\omega_O}{U_H}\right)^2}} \; . \tag{4.11}$$

Thus the relative fractionation is determined only by the diffusion velocity ω and by the main stream velocity U_H. Eq. 4.11 describes how the different

processes (ionisation and diffusion) influence the fractionation: with a larger ionisation rate we get a higher fractionation, while with a higher collision rate, i.e. higher coupling between the minor constituent and hydrogen, a lower diffusion velocity and a lower fractionation are obtained. From this equation we also get a description of the velocity dependence: a lower velocity of the hydrogen background gives an higher FIP effect, with the limit situation of negligible hydrogen velocity and a fractionation given by the ratio between the diffusion velocities.

Chapter 5

The hydrogen background

In order to study the fractionation for minor constituents, a hydrogen background model is needed. Since the fractionation is believed to be related to the ionisation processes, it is important to focus on the altitude where this ionisation takes place. Hence, both the slab thickness and the slab location are chosen with respect to this criterion.

In this work we study the fractionation related to fast solar wind. This means that the background model describes a dynamic atmosphere with a given net hydrogen particle flux. The observed fast solar wind flux at 1 AU is $\Phi_{1AU} \approx 2 \times 10^{12}$ m^{-2} s^{-1}. Assuming flux conservation from the sun's surface to 1 AU radius, we get

$$f\ r_{1AU}^2\ \Phi_{1AU} = r_S^2\ \Phi_S, \tag{5.1}$$

that results in

$$\Phi_S = f\ \Phi_{1AU} \frac{r_{1AU}^2}{r_S^2}, \tag{5.2}$$

where the parameter f represents a geometry factor that describes different areal expansions. Using the values $r_{1AU} = 1.496 \times 10^{11}$ m and $r_{SUN} = 6.96 \times 10^8$ m, we get $\Phi_{SUN} = f \times 9.24 \times 10^{16}$ m^{-2} s^{-1}.

We choose three values for the geometry factor $f = 1$, $f = 20$ and $f = 100$. $f = 1$ represents the radial expansion geometry. $f = 20$ is the most probable value following the work of Byhring et al. (2008) (model F1), based on measured Doppler shift of minor ion spectra lines from the transition region and the corona. $f = 100$ is the geometry factor used by Peter (1998). These three models are be called "L","M" and "H" respectively.

The slab thickness is 1000 km and the chosen linear temperature profile is shown in Fig. 5.1

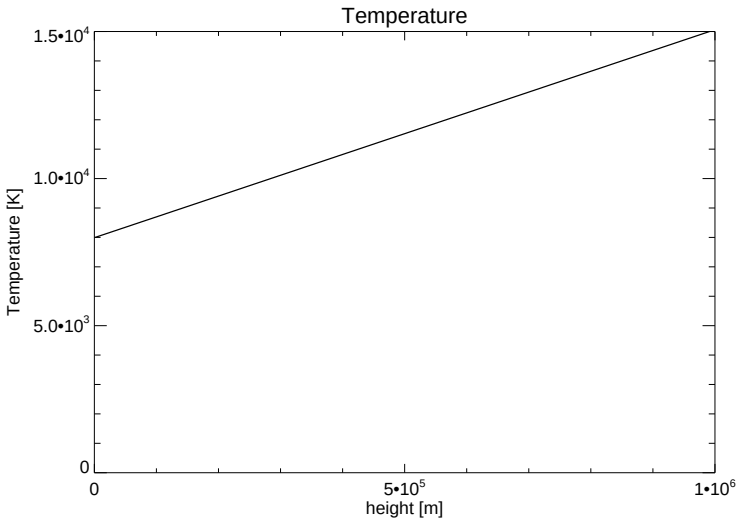

Figure 5.1: *The chosen linear temperature profile.*

5.1 Boundary conditions

In order to repeat the calculation by Peter (1998), we build a model similar to the background described by Peter and Marsch (1998), using almost the same boundary conditions.

At the lower boundary, the neutral hydrogen density is assumed to be 8×10^{16} m^{-3}. The gas streaming up through the lower boundary is set to be ca 2% ionised. This condition does not constrain the ionisation degree to have a fixed value on the first grid point.

The photoionisation rate at the top of the layer is set to be $R_{Hp} = 0.014$ s^{-1} (Peter and Marsch, 1998). The condition of a solar wind stream through our atmosphere is imposed via the proton velocity at the upper boundary. The flux takes three different values for the three different cases L, M and H. The neutral hydrogen and ionised velocities at the top are forced to be equal.

In table 5.1 the values for all the physical parameters are shown.

5.2 Results

We run the code from an initial condition, where the gas is uniformly 1% ionised and the neutral hydrogen profile follows the hydrostatic equilibrium, until we have reached the steady state (10^4 s).

Lower boundary:	Total density	$N_0 = 8 \times 10^{16}$ m^{-3}
	Ionisation degree	0.018
Upper boundary:	Ionisation rate	0.014 s^{-1}
	Velocity	$u_H = u_p$
	Total flux	$\Phi_H = 9 \times 10^{16}, 2 \times 10^{18}, 9 \times 10^{18}$ m^{-2} s^{-1}

Table 5.1: *The boundary conditions used for the background model. Only the fixed boundary conditions are reported.*

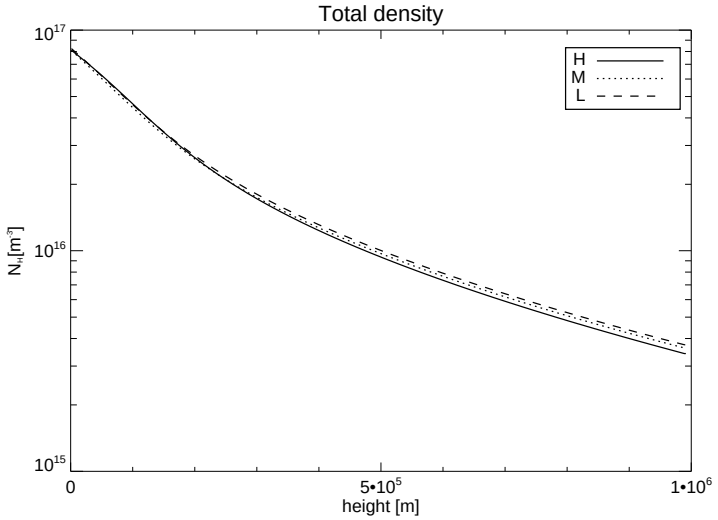

Figure 5.2: *The total hydrogen density profile.*

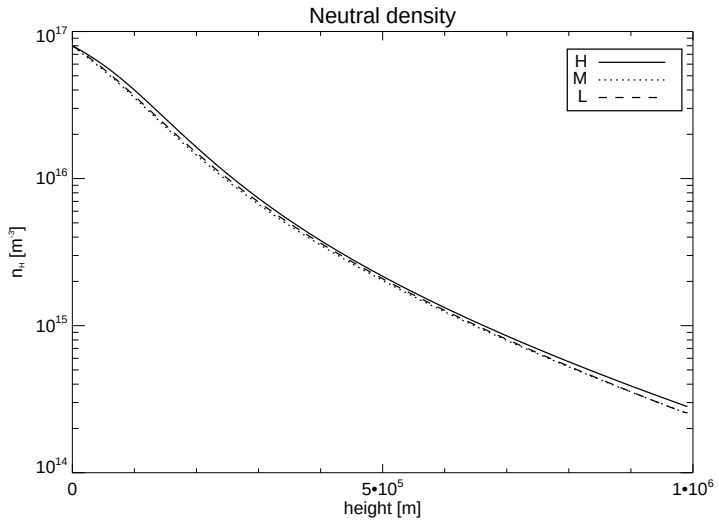

Figure 5.3: *The neutral hydrogen density profile.*

The sum of the neutral and ionised hydrogen density profiles is shown for the three wind fluxes H, M and L in Fig. 5.2. The density decreases slightly with increasing flux, but the differences between the densities in the three cases are very small.

The neutral and ionised density profiles are shown in Fig. 5.3 and Fig. 5.4, respectively. For neutral hydrogen the L and M profiles are almost equal while the H profile has a bit higher density. The proton densities do not follow a monotone profile, but reach a top near $z = 2 \times 10^5$ m. The differences between the H, M and L profiles are bigger than in the neutral case, and the higher flux the lower density.

The ionisation rates for the H, L and M cases are shown in Fig. 5.5. All the profiles have a monotone behaviour, with a rate increasing more rapidly in the lower part of the slab. The figure shows the sum of the radiative and collisional ionisation rates, but the latter constitutes less than 5% of the total rate.

Fig. 5.6 shows the ionisation degree for the three flux cases. These profiles follow the ionisation rates shown in Fig. 5.5 and justify our choice for the slab thickness, since we are interested in studying the ionisation area. While the L and M cases have the same ionisation degree, the H case differs from the other two with an almost constant gap.

If one supposes a static situation with zero particle flux for both neutral

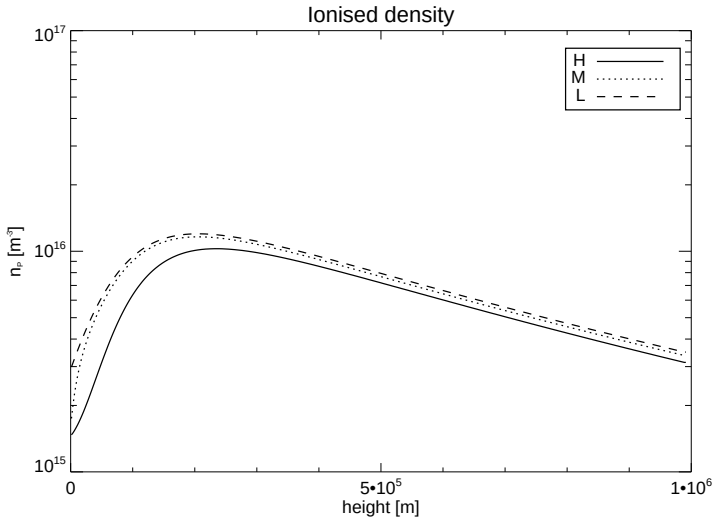

Figure 5.4: *The proton density profile.*

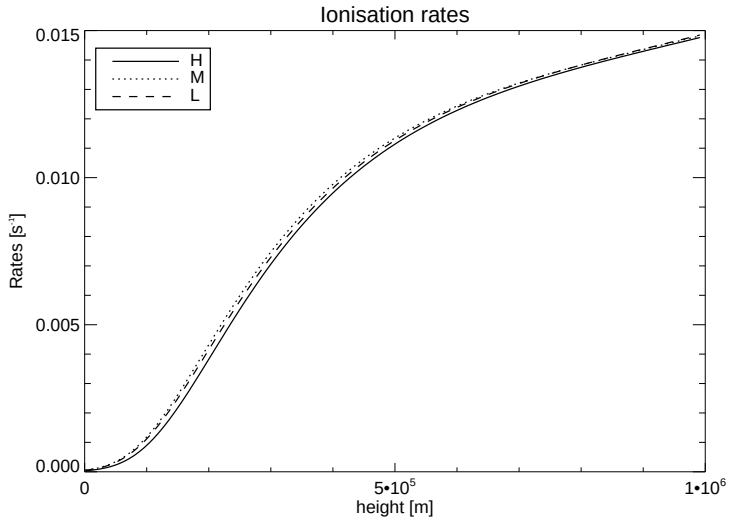

Figure 5.5: *The ionisation rates.*

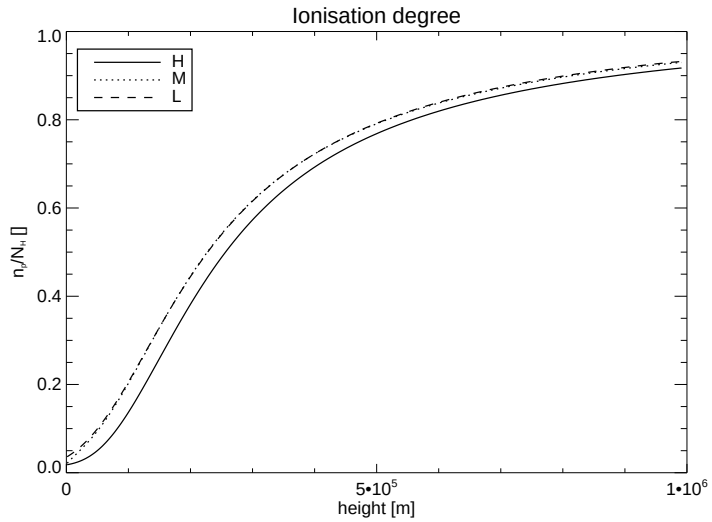

Figure 5.6: *The ionisation degree.*

and ionised hydrogen, equation 2.1 for protons becomes

$$0 = n_1 \; P_{12} - n_2 \; P_{21}, \tag{5.3}$$

which gives an ionisation degree at equilibrium, given by

$$\frac{n_2}{n_1 + n_2} = \frac{P_{12}}{P_{12} + P_{21}}, \tag{5.4}$$

where the indexes 1 and 2 are the same as in eq. 2.1. The actual ionisation rates are compared with the ionisation equilibrium result (eq.5.4) in Fig. 5.7. We see that both the L (left panel) and M case (centre panel) are in ionisation equilibrium, while the ionisation degree for the H case is slightly lower than the equilibrium ionisation degree.

The hydrogen gas velocities for the L, M and H cases are shown in Fig. 5.8. In the H case (right panel), the neutral and ionised velocities are almost equal, and increase from ca 100 to over 2300 m s^{-1}. In the M case (centre panel) the ionised velocity starts from a bit lower value at the bottom, but reaches the neutral velocity almost at once. Both neutral and ionised velocities vary from ca 20 m s^{-1} at the bottom to over 550 m s^{-1} at the top. In the L case (left panel) the velocities vary from around 0 to ca 25 m s^{-1}. This case shows the biggest relative difference between neutral and ionised hydrogen. In fact the protons have a velocity profile that starts from negative values at the bottom of the layer, while the neutral velocity is positive throughout the layer.

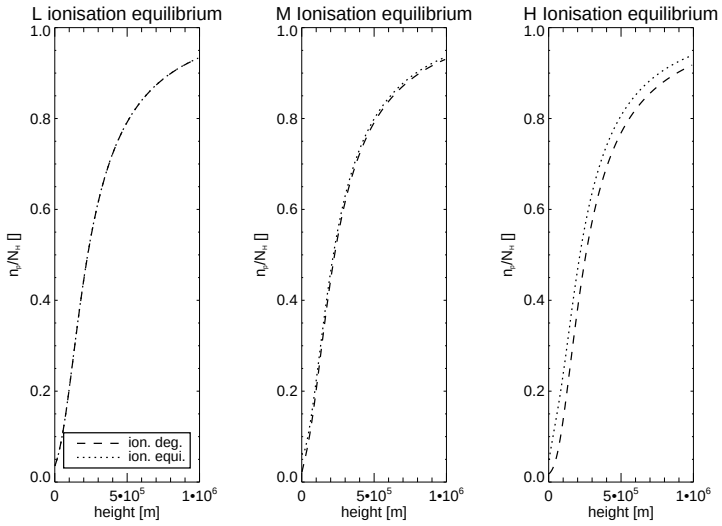

Figure 5.7: *The ionisation degree plotted together with the ionisation degree at equilibrium.*

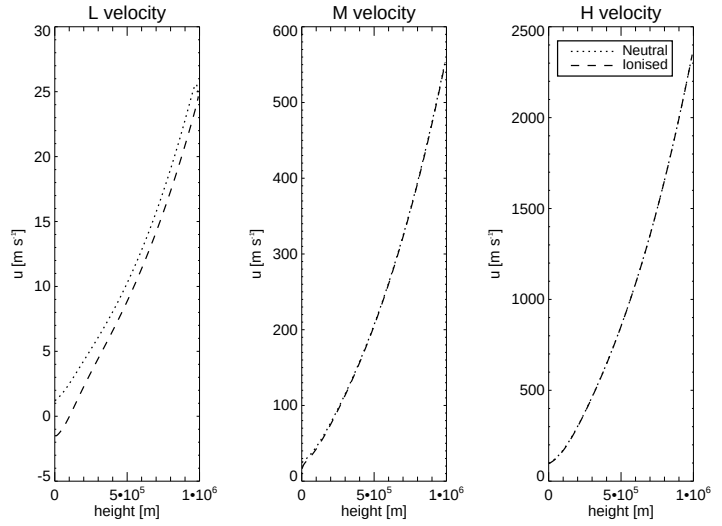

Figure 5.8: *The neutral and ionised hydrogen velocity profiles.*

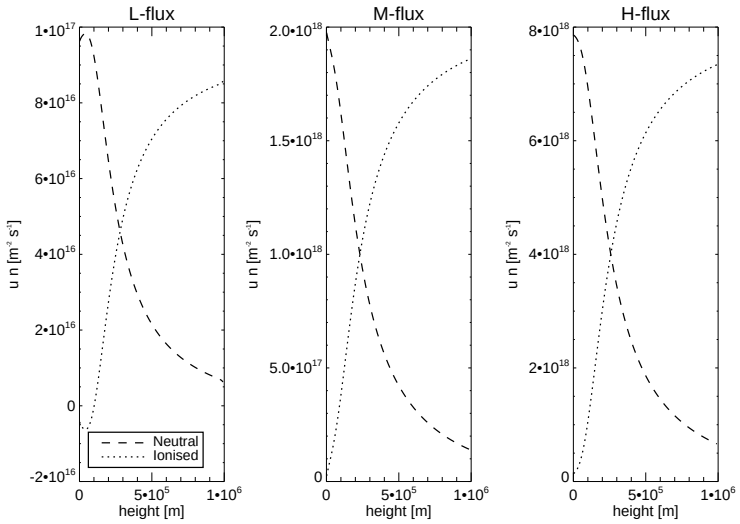

Figure 5.9: *The neutral and ionised hydrogen flux profiles.*

Fig. 5.9 presents the neutral and ionised hydrogen fluxes plotted for the L case (left panel), M case (centre panel) and H case (right panel). Obviously, since we run the code until steady state is reached, the total flux is constant throughout the slab. The M and H differs only by a scale factor. The L case shows instead a negative proton flux near the lower boundary.

Figs. 5.10 and 5.11 show the force equilibrium for neutral (upper panel) and ionised hydrogen (lower panel) in the H and L case. Writing the forces contributions divided by the mass the force equilibrium becomes (see eq. 2.2):

$$-\frac{1+\frac{q_i}{e}}{m_i n_i}\frac{\partial}{\partial z}(n_i kT) + g + \sum_{j\neq i} k_{mt} n_j (u_j - u_i) = 0, \tag{5.5}$$

where we have neglected the advective term and the ionisation term because of their low contributions when the force balance is reached. The H and L neutral plots show approximately the same behaviour, with an upward pressure gradient force balanced by the sum of gravity and collisions. The collisions constitute a friction term between neutral hydrogen and protons, and therefore, by adjusting the velocity gap between neutral and ionised hydrogen, provide for the balance. While the gravity is obviously constant over the slab, the pressure gradient force reaches a maximum ca at 2×10^5 m, to slowly decrease at higher altitudes. As long as the collisional friction is significantly different from zero (lower part of the slab) the force balance is far from the hydrostatic equilibrium.

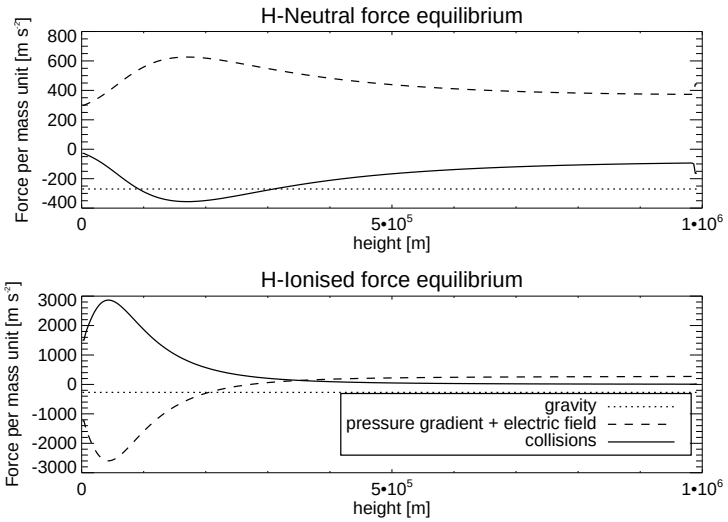

Figure 5.10: *The force equilibrium for neutral and ionised hydrogen, H case.*

The picture is quite different for protons (lower panel). Here the pressure gradient, which has to be added to the electric field, provides a downward force which is balanced by a positive collisional friction. In the lower part of the slab, gravity is, by comparison, almost negligible. In the upper part the pressure gradient force gives a positive contribution, balancing gravity in hydrostatic equilibrium. The pressure gradient in the L case increases monotonously, while in the H case it decreases to a minimum at ca 5×10^4 m and then it increases.

5.3 Discussion

Since the flux is subsonic, the density profile remains almost unchanged for the different flux cases.

The ionisation degree for all the models follows the same profile as the photoionisation rate, and the ionisation degree is close to ionisation equilibrium. However, the departure from the ionisation degree at equilibrium gets bigger with higher fluxes, while the ionisation degree decreases.

This fact is easily understandable by using the *ionisation length* concept. Let's say that a neutral gas needs a given time τ_{ION} to get ionised up to the ionisation equilibrium, where this ionisation time is given by the ionisation degree at equilibrium divided by the ionisation rates. If the neutral gas

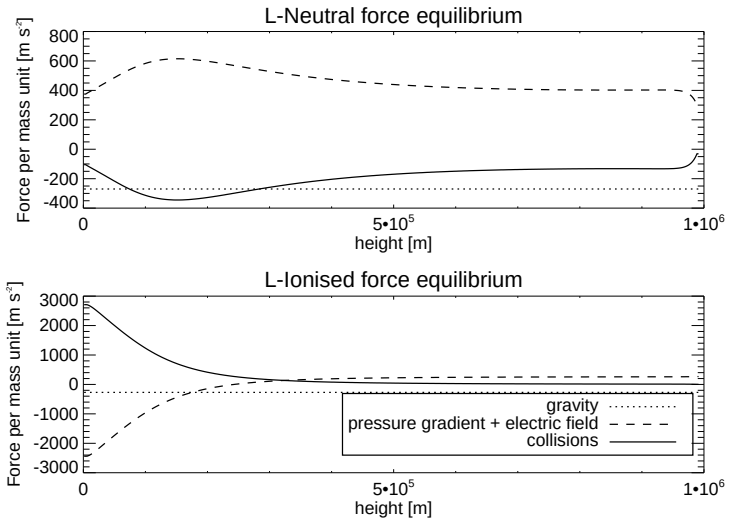

Figure 5.11: *The force equilibrium for neutral and ionised hydrogen,L case.*

streams through the layer with a velocity U, it will cover a distance L_{ION}, before it reaches the ionisation equilibrium, which is given by: $L_{ION} = U\ \tau_{ION}$. So the higher wind flux we have, the bigger the ionisation length becomes, and a bigger gap between ionisation degree and equilibrium can be expected. For example, by comparing the ionisation degree (dashed line in the right panel of Fig. 5.7) with the ionisation degree at equilibrium (dotted line) in the H case, we get that the former is delayed with respect to the latter by a distance $\Delta z \approx 5 \times 10^4$ m. This value is comparable with the calculated ionisation length at the first grid point, $L_{ION} \approx 1 \times 10^5$ m. In the L case this effect is not visible at all. The negative and low positive proton velocities near the lower boundary force the recently ionised hydrogen to stop. So, even if the ionisation process takes a long time, the protons can accumulate until they reach the ionisation equilibrium; in other words the *ionisation length* approximation makes no sense if the proton velocities are too different from the neutral hydrogen velocities. This effect plays an even more important role for the minor constituents. Furthermore, the fact that in the L case the ionisation equilibrium is reached already at the first grid point while in the H case the ionisation process is delayed, explains the large difference in proton density near the lower boundary between the H and L case (see Fig. 5.4).

The relative difference between neutral and ionised hydrogen velocity changes for L, M and H, but by studying the absolute difference one can see that this difference does not vary too much between the three cases.

The neutral hydrogen velocity is bigger than the proton velocity because

the ionisation process leads to a density profile with a positive pressure gradient force, higher than what gravity manages to balance. This upward force increases the neutral hydrogen velocity until the force is balanced by collisional friction. For protons we have a similar dynamic: the ionisation process leads, in the lower part of the layer, to an increasing density profile and a subsequent negative pressure gradient force. In this case too, the collisional friction balances this downward pressure gradient. In the upper part of the layer, hydrogen is ionised to a high percent and the pressure gradient force for protons becomes positive.

This relationship can also be studied analytically by supposing force balance between gravity, pressure (and electric field) and collisions. Subtracting eq.5.5 (written for protons) from the respective hydrogen equation and neglecting temperature gradient with respect to density gradient we obtain:

$$-\frac{kT}{m_H}\left(\frac{d}{dz}log\ n_H - 2\frac{d}{dz}log\ n_P\right) + k_{mt}(u_p - u_H)N_H = 0, \qquad (5.6)$$

where the index H refers to neutral hydrogen and p to protons. $N_H = n_H + n_p$ is the total hydrogen density. We finally obtain that

$$u_p - u_H = \frac{k}{k_{mt}m_H}\ \frac{T}{N_H}\ \frac{d}{dz}\left(log\frac{n_H}{n_p^2}\right), \qquad (5.7)$$

which clearly shows how velocity differences depend only on density profiles and on temperature profile. Eq. 5.7 states also that a non-homogeneous ionisation degree leads to a difference between hydrogen and proton velocity. By a comparison between the analytical and numerical model it results that eq. 5.7 is a very good approximation and permits a correct understanding of the force equilibrium in the hydrogen background.

The obtained difference between neutral and ionised hydrogen velocity is therefore coupled with the density profiles and finally with the ionisation degree. Since the L, M and H cases have a very similar ionisation degree, also the absolute differences between ionised and neutral velocities are similar. This result also tells us that a lower boundary condition that forces the neutral and ionised velocity to be equal should not be adopted together with a varying ionisation degree.

Chapter 6

The minor constituents

We now solve the equation 2.1 and 2.2 for the minor constituents oxygen, neon, silicon, magnesium and iron, until steady state is reached. This will require different running times for the code since every model has its characteristic evolution time.

Each element is studied with three different backgrounds L, M, and H, which correspond to three different choices of the geometry factor f.

For some minor constituents the ionisation-recombination dynamic is driven by radiative processes (see section 2.1.1 and α_r in section 2.2.2) while for other elements also the collisional processes are important (see section 2.1.2 and α_d in 2.2.2). For oxygen charge exchange is the dominant channel for the ionisation process.

We run the code from an initial condition where the minority gas is 0.1% ionised with an absolute abundance $A_{abs} = 5 \times 10^{-4}$ uniform over the slab. This gives a start distribution that follows the same behaviour as the background hydrogen profile.

6.1 Boundary conditions

No condition constrains the velocities for the minor constituents, i.e. they are determined by the force balance at lower and upper boundary.

At the lower boundary, in order to simplify comparisons, $A_{abs} = 5 \times 10^{-4}$ for all the minor constituents.

If the velocities near the lower boundary are positive the ionisation degree of the gas streaming through the lower boundary is set to 0.01, otherwise the density values on lower boundary are calculated via an upwind differencing scheme.

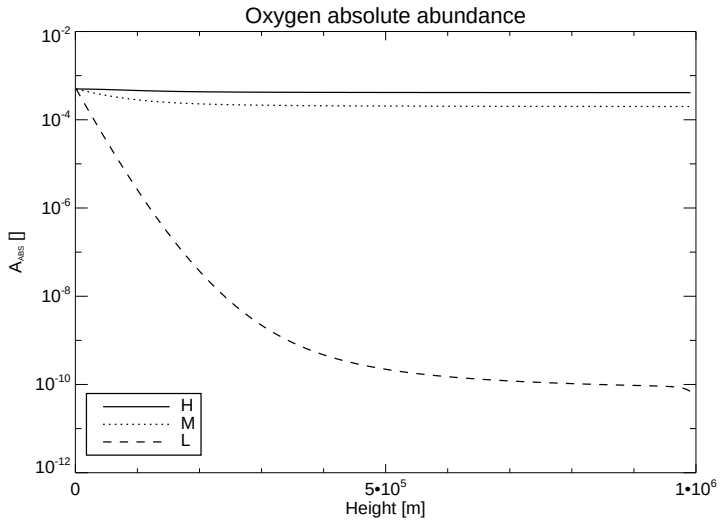

Figure 6.1: *The oxygen absolute abundance.*

6.2 Oxygen

Oxygen has a peculiar behaviour because it is coupled to hydrogen via the very effective charge transfer channel.

Both the radiative and collisional ionisation and recombination can be neglected with an error not bigger than 1%.

We run the code for 10^4 s for the H case, 10^5 s for the M, and 5×10^6 s for the L case, in order to reach the steady state.

6.2.1 Results

Fig. 6.1 shows the absolute abundances for the H, L and M cases. The H and M cases show a very slowly decreasing absolute abundance with altitude. In the H case the abundance decreases from the boundary/initial value 5×10^{-4} to 4×10^{-4} in the lower part of the slab and then it flattens out almost completely. The same behaviour is shown in the M case where A_{abs} decreases to ca 2×10^{-4}. The L case presents a radically different picture where the absolute abundance is reduced by a factor of 10^7. This abundance decreases exponentially up to $z = 3 \times 10^5$ m but flattens out throughout the rest of the grid.

Since the initial condition has a homogeneous absolute abundance, the time needed to obtain the steady state increases radically from the H to the L case.

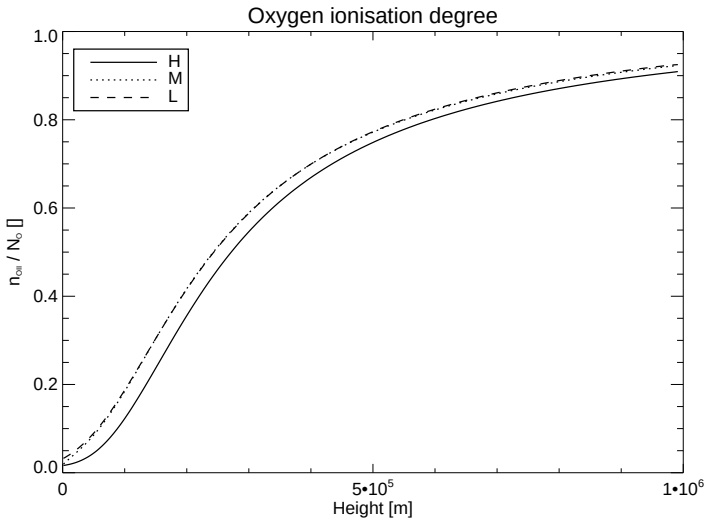

Figure 6.2: *The oxygen ionisation degree.*

The oxygen ionisation degree is presented in Fig. 6.2, showing an ionisation degree very similar to hydrogen (see Fig. 5.6). The L and M cases have the same ionisation degree profile, while the H case presents a slightly lower ionisation degree.

The velocities for neutral and ionised oxygen, plotted together with the proton velocities, are shown in Fig. 6.3. In the H case (right panel), the proton and the ionised oxygen velocities are coincident, and the neutral velocities are also very similar to them. In the M case (centre panel), the difference between the ionised and neutral oxygen velocities becomes more appreciable, while the ionised oxygen and protons velocities are still coupled. The L case (left panel) shows a quite different picture where the neutral oxygen velocities decrease from zero at the lower boundary to quite high negative values. The ionised velocities rise from a negative value at the lower boundary and follow the proton velocities for the rest of the grid.

The fractionation process for a minor constituent X can be studied (see eq.4.10) by introducing the average velocity U_X:

$$U_X = \frac{n_n u_n + n_i u_i}{N_X}, \tag{6.1}$$

where, the indexes n and i refer to the neutral and ionised specie. Fig. 6.4 shows the ratio between the oxygen and hydrogen average velocities. For all the three flux cases the oxygen velocity at lower boundary is lower than the hydrogen velocity, and then it increases. The oxygen and hydrogen velocities

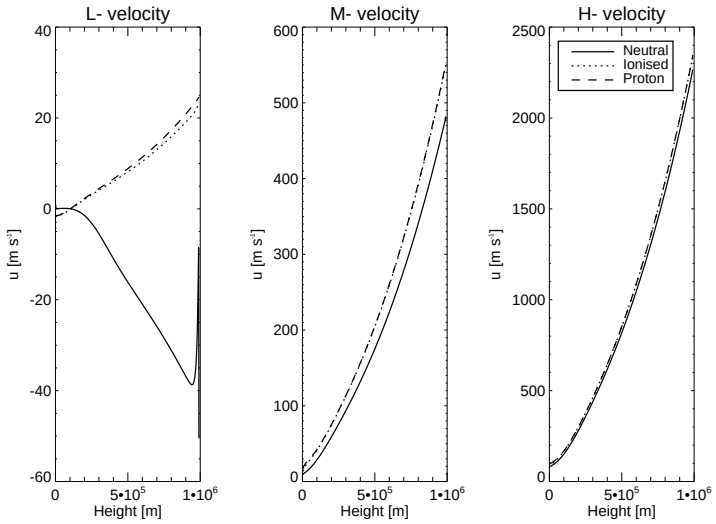

Figure 6.3: *The neutral and ionised oxygen velocity profiles.*

at the upper border are coupled for the H and M cases, while the L case shows an oxygen velocity that remains relatively much lower than the hydrogen one.

By studying the velocity difference between ionised and neutral oxygen (left panel of Fig. 6.5) we see that this difference remains almost unchanged by varying the flux. The right panel of Fig. 6.5 shows the difference between the ionised oxygen and proton velocities, giving a measurement of how much these are coupled. The departure of the ionised oxygen velocities from protons is, except at lower altitudes, very similar in the three cases.

Fig. 6.6 shows the neutral and ionised oxygen flux for the three cases. The net flux is $\approx 3 \times 10^{15}$ m^{-2} s^{-1} for the H case, $\approx 4 \times 10^{14}$ m^{-2} s^{-1} for M but only $\approx 5 \times 10^{6}$ m^{-2} s^{-1} in the L case. In the L case both the neutral and ionised flux fall to zero already at $z = 10^5$ m, and below this altitude the neutral flux is positive and the ionised is negative. By dividing the net oxygen flux with the net hydrogen flux we get the relative net flux for oxygen. In the H case the relative net flux is $\approx 4 \times 10^{-4}$, for M $\approx 2 \times 10^{-4}$ and for the L case the flux is $\approx 6 \times 10^{-11}$. The net relative flux gives approximately the same value as the absolute abundance at the top of the slab (see Fig. 6.1) and it is therefore a good way to study how much of the minor constituent is dragged out by hydrogen.

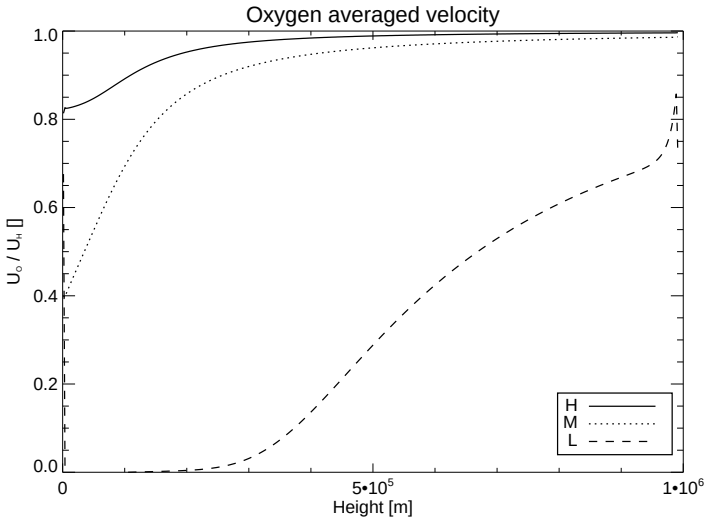

Figure 6.4: *The ratio between the oxygen and hydrogen average velocities.*

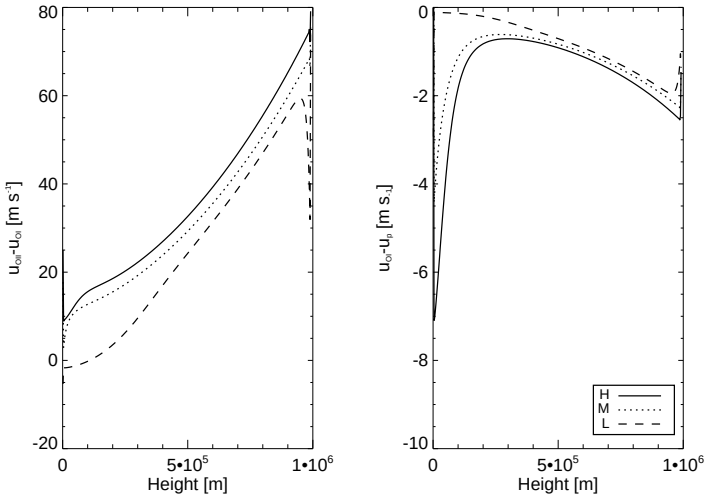

Figure 6.5: *The velocity difference between ionised and neutral oxygen (left panel). The velocity difference between ionised oxygen and protons(right panel)*

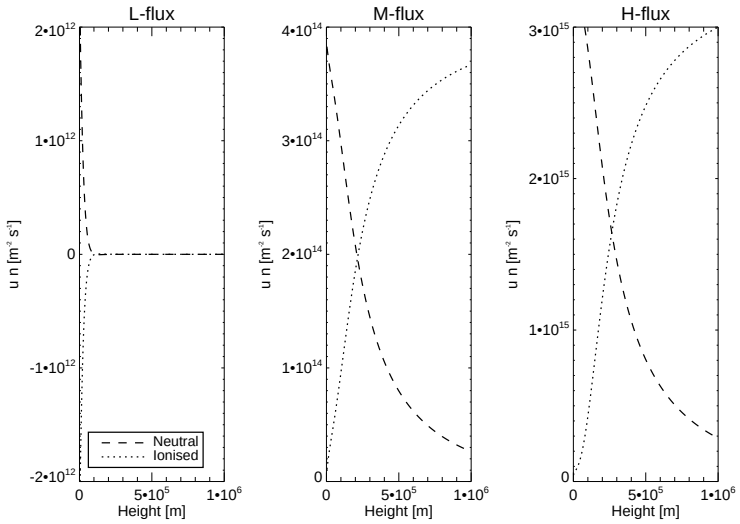

Figure 6.6: *The neutral and ionised oxygen flux.*

Turning to the force balance, eq. 2.2 for oxygen becomes:

$$-\frac{1}{m_i n_i}\frac{\partial}{\partial z}(n_i kT)+g+\frac{n_j u_j\ P_{ji}-n_i u_i P_{ij}}{n_i}-\frac{q_i}{e m_i n_p}\frac{\partial}{\partial z}n_p kT$$
$$+\nu_{iH}(u_H-u_i)+\nu_{ip}(u_p-u_i)=0\ , \qquad (6.2)$$

where we have again neglected the advective term, and the ionisation term is dominated by charge exchange. Charge exchange acts as a friction term between neutral and ionised oxygen, while collisions reduce the velocity difference between oxygen and hydrogen.

The force equilibrium for neutral and ionised oxygen for the H case is shown in Fig. 6.7. The collision term constitutes a positive force for both neutral and ionised oxygen. Because of the very effective coulomb collisions, this term is much larger for ionised oxygen. For ionised oxygen all the other forces, gravity, charge exchange and pressure gradient are negative (in the upper part of the slab pressure becomes positive but almost zero) in order to balance collisions. For neutral oxygen collisions are much less effective and above 2×10^5 m they are substituted by charge exchange as principal upward force. The pressure gradient is almost totally negligible.

The force equilibrium for the L case, shown in Fig. 6.8, presents a different picture. Here the pressure gradient is the most important positive force in the lower part of the layer. For the neutral gas the hydrostatic equilibrium is reached at lower altitudes, while in the upper part the charge exchange

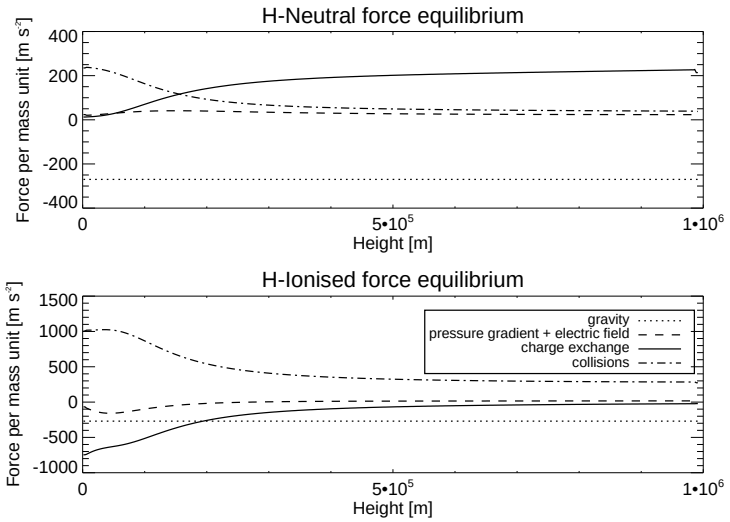

Figure 6.7: *The oxygen force equilibrium in the H case.*

friction balances gravity. In the lower part of the slab, the L case shows, relative to the H case, a much lower collisional friction. This friction becomes comparable with the pressure gradient and the charge exchange.

6.2.2 Discussion

The oxygen ionisation degree is almost the same as hydrogen. This fact can be easily understood by studying the charge exchange process. Since C_{ion} and C_{rec} from eq.2.28 differ by less than 10%, the ionisation degree at equilibrium can be written as:

$$\frac{n_i}{n_i + n_n} = \frac{n_p}{n_H \frac{C_{rec}}{C_{ion}} + n_p} \approx \frac{n_p}{n_H + n_p}. \tag{6.3}$$

In all the flux cases oxygen is depleted with respect to hydrogen. In the H and M cases, however, the absolute abundance is almost constant and the oxygen is dragged up by hydrogen. The absolute abundance of oxygen in the L cases falls by a factor of 10^7.

The ionised oxygen velocity is almost totally coupled with the proton velocity and the gap between them does not vary too much between the H, M and L cases.

From the force equilibrium for ionised oxygen in both the L and the H case we see that on the upper part of the slab the collisional friction is the

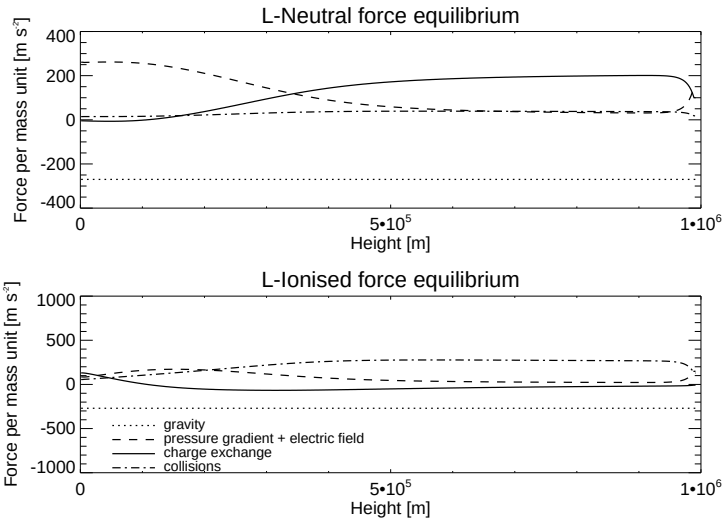

Figure 6.8: *The oxygen force equilibrium in the L case.*

only force that balances gravity. The difference between the ionised oxygen and proton velocities is thus given by:

$$u_i - u_p = \frac{g}{\nu_{2p}}, \tag{6.4}$$

where ν_{2p} is the collisional rate for Coulomb collisions. Eq. 6.4 explains why this velocity difference has the same profile for the three flux cases except at lower altitudes, where the pressure and the charge exchange are no longer negligible.

In order to obtain an absolute enrichment the element average velocity (eq. 6.1) at the left boundary must be larger than the hydrogen average velocity (see eq. 4.10). Neither the ionised nor the neutral oxygen velocities are larger than the hydrogen velocities and no enrichment is therefore obtained.

One of the largest difference for neutral oxygen between the H and L case is that collisions with hydrogen are significant for the H case at lower altitudes, while they are negligible for the L case, where the pressure gradient balances gravity. In order to understand the reasons of this difference we study the time development for the neutral oxygen force equilibrium at lower altitudes. Initially all the cases, L, M and H, reach the same free fall equilibrium where collisions with neutral hydrogen balance gravity, giving

$$u_H - u_n \approx -\frac{g}{\nu_{nH}}. \tag{6.5}$$

This value is nearly constant for the three flux cases and gives a velocity difference of about 20 m s^{-1}. While in the H case the hydrogen velocity at the lower boundary is ≈ 100 m s^{-1}, in the L case u_H is just ≈ 1 m s^{-1} . In order to obtain a collision force able to balance gravity, the neutral oxygen velocity must be negative and with falling oxygen a pressure gradient can be build.

The hydrostatic equilibrium in the lower part of the slab for the L case leads to a strongly decreasing abundance.

6.3 Low FIP elements

6.3.1 Silicon

In the ionisation process the radiative ionisation rate is dominant by a factor of 10^3 over the collisional rate at the bottom, while at the top of the layer they become of the same order of magnitude. In the recombination process the dielectronic recombination rate is a factor of 10 smaller than the radiative recombination rate at the bottom, but dominates by a factor of 7 over the radiative at the top.

We run the code for 5×10^6 s, 2×10^4 s and 1×10^4 s in the L, M and H case respectively in order to reach a steady state.

The incoming gas has an ionisation degree of 1% while the gas at the first grid point is 99% ionised. Some dynamic (see chapter 7) caused by this huge difference lead to a lower boundary density value that does not behave like a fixed boundary. Thus, in order to compare the abundances for different elements and for different flux cases, it has been necessary to make a normalisation of the density values.

Fig. 6.9 shows the absolute abundance for silicon for the L case (left panel) and for the M and H cases (right panel). The absolute abundance decreases with height for all the cases. The decreasing factor for the H and M cases is not larger than one third of the lower boundary value, whereas for the L case the abundance decreases by a factor of 10^{10}.

In Fig. 6.10 the silicon relative abundance is shown. In the H and M cases the relative abundance shows an increasing behaviour that leads to a relative enrichment with respect to oxygen. The increasing factor is larger for the M case. The L case, on the other hand, shows a relative abundance decreasing by a factor of 10^6, reaching a minimum at $z = 10^5$ m, and increasing again by a factor of 10^3.

The ionisation degree of silicon, presented in Fig. 6.11, is almost totally constant for the three flux cases and describes a fully ionised gas. Even in

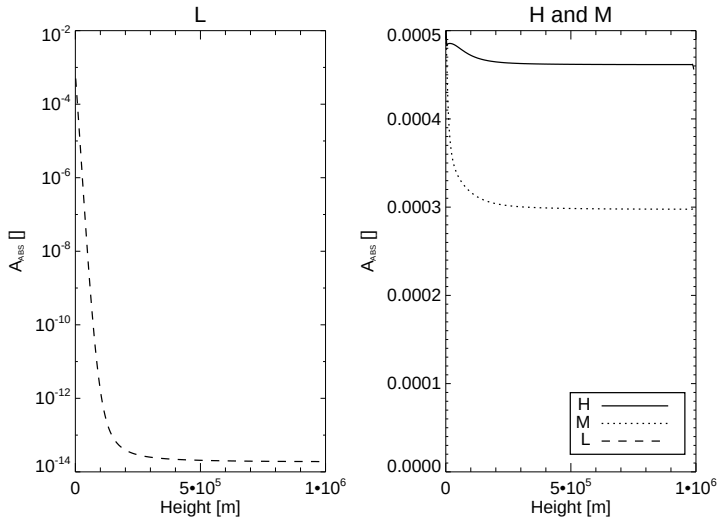

Figure 6.9: *The silicon absolute abundance.*

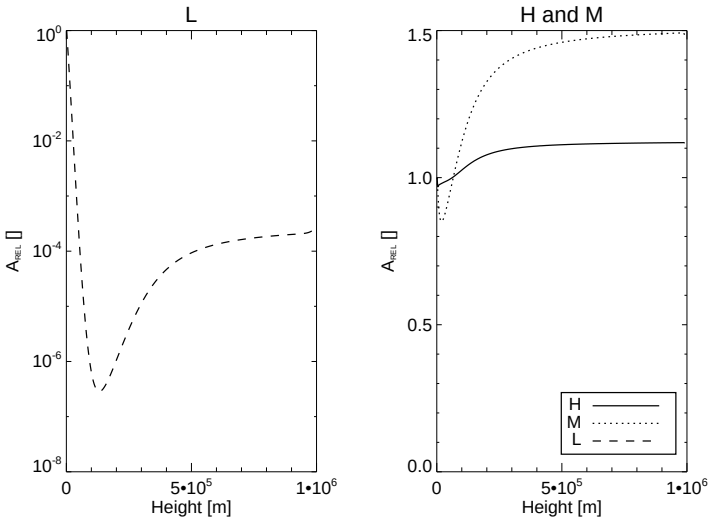

Figure 6.10: *The silicon relative abundance.*

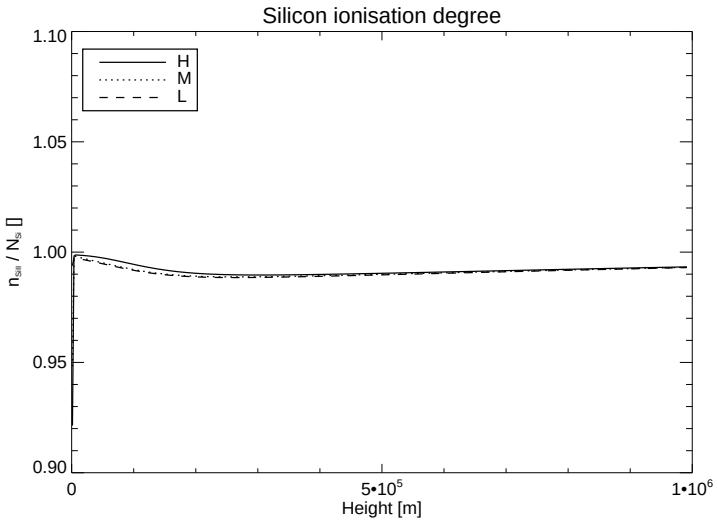

Figure 6.11: *The silicon ionisation degree.*

the H case it is not possible to see any *ionisation length* effect (see section 5.3). That is because the ionisation rate is too large and consequently the ionisation length too short ($\approx 10^2$ m) with respect to the slab dimension (the grid spacing $dz = 2.5 \times 10^3$ m). A detailed analysis of this problem is presented in section 7.2.1.

Fig 6.12 shows the neutral and ionised velocity profiles for the L (left panel), M (centre panel), and H case (right panel). As in the case of oxygen the H and M cases show both ionised and neutral velocities increasing with altitude, while in the L case the neutral velocities fall to high negative values. However, with such a high ionisation degree the neutral velocities do not contribute to the overall flux.

The ratio between the silicon average velocity U_{Si} and the hydrogen average velocity is shown in Fig. 6.13. The velocity value at the lower boundary is less than one for all the cases and no absolute enrichment is therefore obtained.

Since silicon is fully ionised we are only interested in the SiII force equilibrium, for which the H case is shown in Fig. 6.14. Throughout the slab, gravity is balanced by collisions with hydrogen.

6.3.2 Magnesium

The ratio between the collisional and radiative ionisation rates, $\frac{C_{ni}}{R_{ni}}$, varies between 2×10^{-3} at the bottom of the layer and 1 at the top. For the

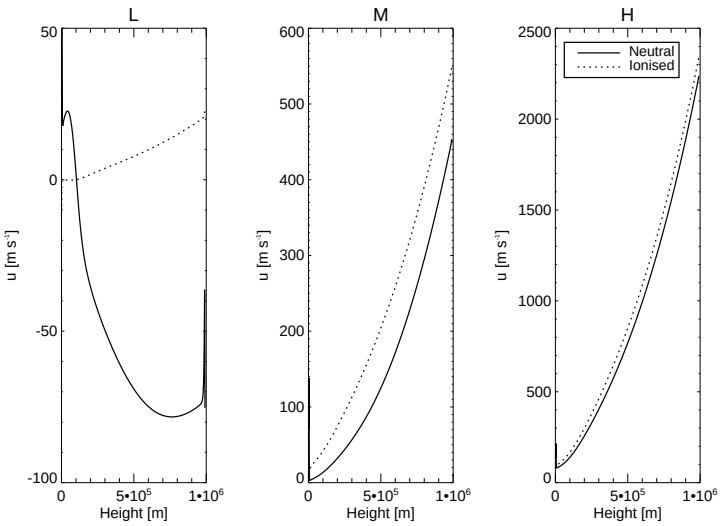

Figure 6.12: *The neutral and ionised silicon velocity profiles.*

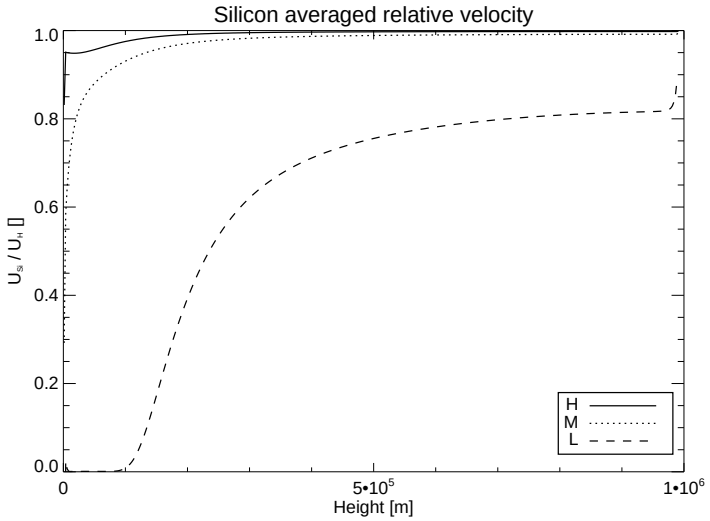

Figure 6.13: *The silicon average velocity.*

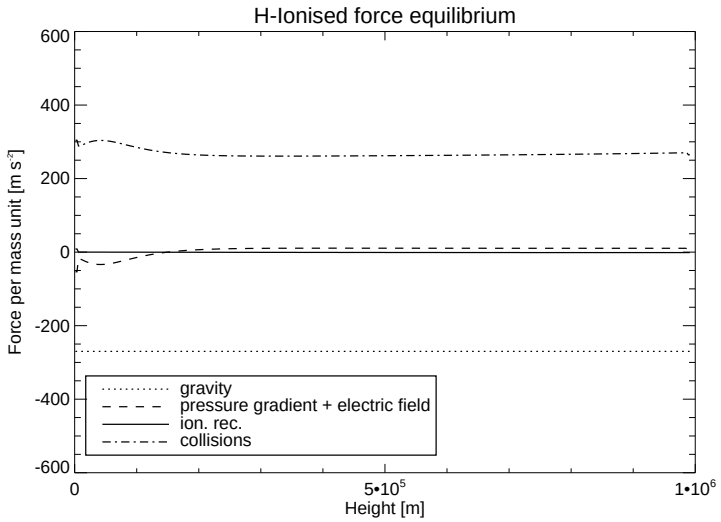

Figure 6.14: *H -Ionised silicon: The force equilibrium.*

recombination process we have that $\alpha_d/\alpha_r \approx 7$ at the bottom and becomes $\approx 9 \times 10^2$ at the top.

The code is run for 2×10^6 s, 1×10^5 s and 1×10^4 s for the L, M and H case respectively, in order to reach the steady state.

Fig. 6.15 shows the magnesium absolute abundance, which follows the same behaviour as silicon. The L case presents a drastic fall by a factor of 10^9 while the H and M have both a slightly decreasing profile.

Also the magnesium relative abundance (Fig 6.16) has the same behaviour as silicon. The L profile reaches a minimum at $z \approx 1 \times 10^5$ m and it then increases. The M and H cases both rise in relative abundance, i.e. an enrichment with respect of oxygen is obtained. The M case presents an higher enriching factor.

As for silicon, the magnesium ionisation degree (Fig 6.17) is almost constant throughout the layer, and around 99%. No *ionisation length* effect is registered.

The magnesium velocity profiles for the L case (left panel), M (centre panel) and H case (right panel) are shown in Fig 6.18. As for silicon the overall flux is only determined by the ionised velocities and the MgI velocities are thus uninteresting. Following the same profiles as oxygen, all the three cases show the MgII velocities increasing with height.

The ratio between the magnesium and hydrogen average velocity is presented in Fig. 6.19. For all the cases the ratio at the bottom is less than one and we therefore do not achieve any absolute enrichment.

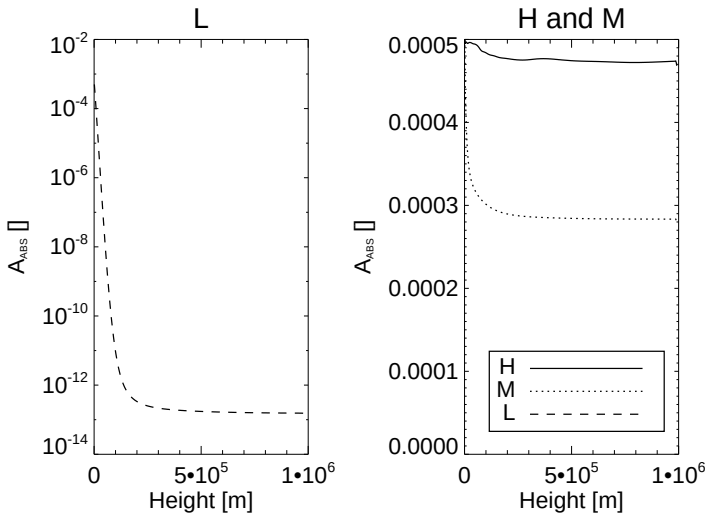

Figure 6.15: *The magnesium absolute abundance.*

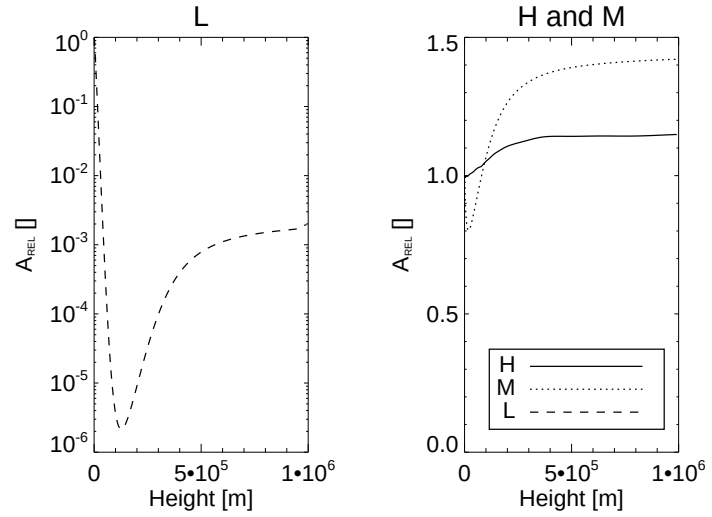

Figure 6.16: *The magnesium relative abundance.*

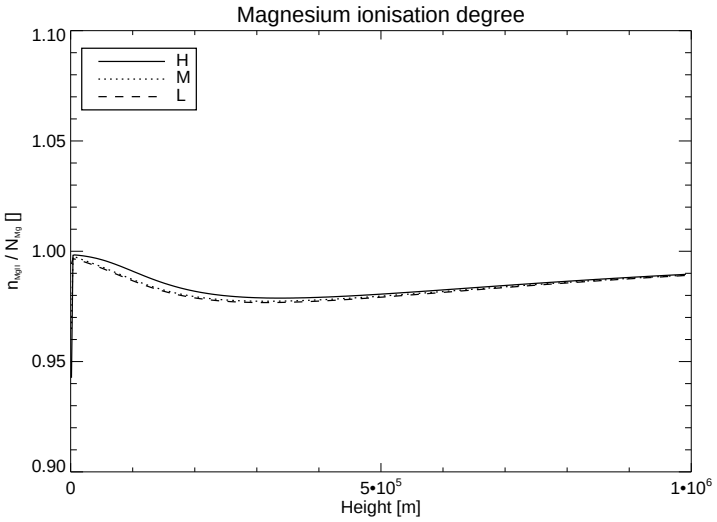

Figure 6.17: *The magnesium ionisation degree.*

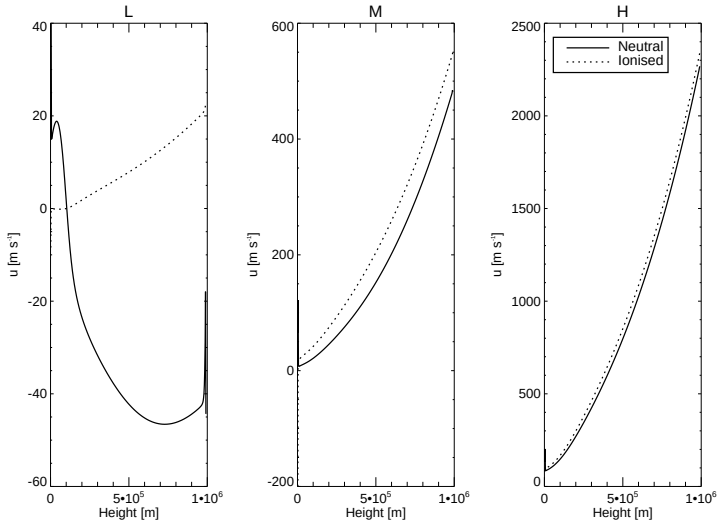

Figure 6.18: *The neutral and ionised magnesium velocity profiles.*

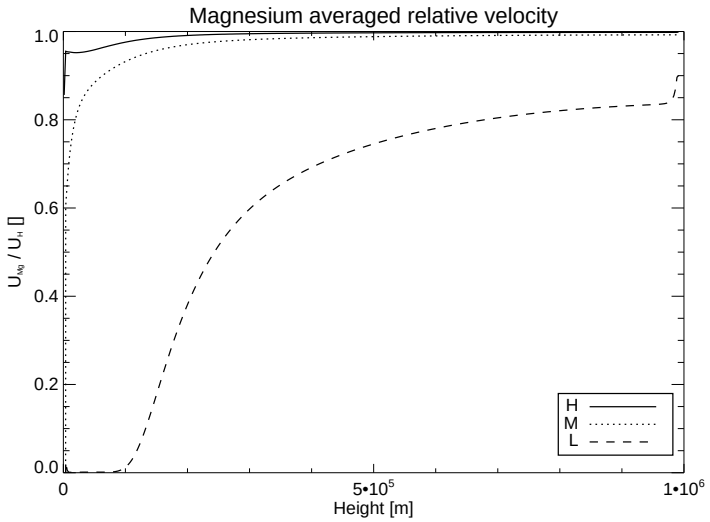

Figure 6.19: *The magnesium average velocity.*

6.3.3 Iron

The ratio $\frac{C_{ni}}{R_{ni}}$ varies between 2×10^{-4} at the bottom of the layer and 0.3 at the top. α_d/α_r varies from 1 at the bottom to 2×10^1 at the top.

The code is run for 3×10^6 s, 1×10^5 s and 1×10^4 s for the L, M and H case respectively, in order to reach the steady state.

The iron absolute abundance is shown in Fig. 6.20. The L case, (left panel), shows a fall by a factor of 10^{18} in the lower part of the slab. The H and M cases present a small decrement, by a factor of 0.1 and 0.3 respectively.

The iron relative abundance is presented in Fig. 6.21. The relative abundance in the L case (left panel) presents a radical fall by a factor of 10^{13} in the lower part of the slab. On the other hand the H and M cases present a rise in the relative abundance.

As for silicon and magnesium, iron is totally ionised already at the first grid point. Also the velocity profiles for iron are almost the same as silicon and magnesium, with an increasing ionised velocity for all the flux cases.

The ratio between the iron and hydrogen average velocity is shown in Fig 6.22. All the cases present an increasing behaviour starting from a value smaller than one, which means that no absolute enrichment is achieved.

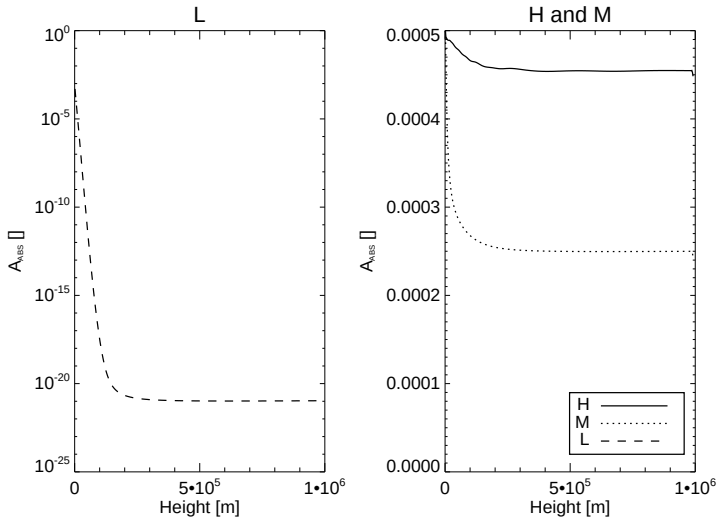

Figure 6.20: *The iron absolute abundance.*

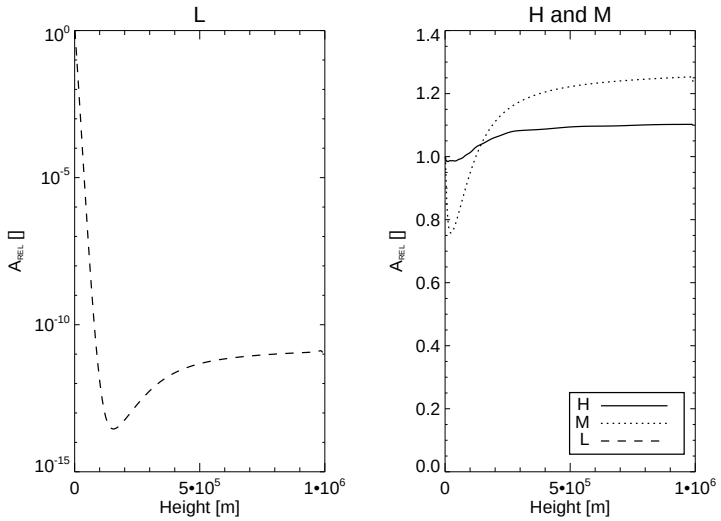

Figure 6.21: *The iron relative abundance.*

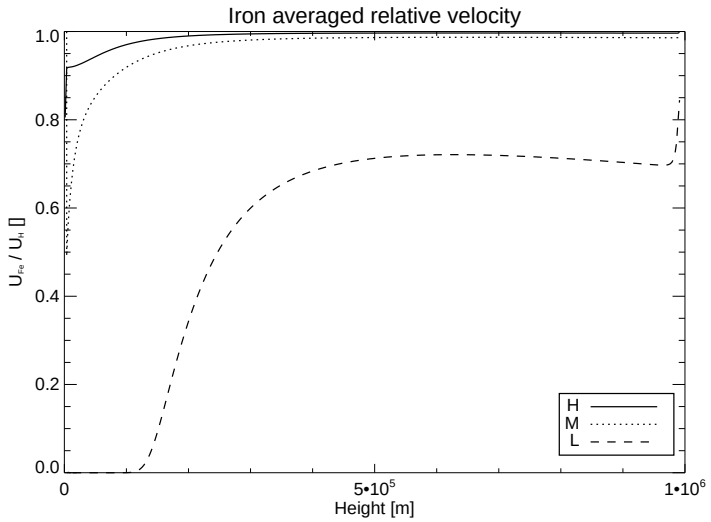

Figure 6.22: *The iron average velocity.*

6.3.4 Discussion

For all the low FIP elements the gas is fully ionised already at the first grid point. This could mean that the grid dimensions are too large with respect to the ionisation space scale. The reason why we chose this grid was to reproduce the results of Peter (1998). Abundances values obtained with a grid with a higher resolution near the lower boundary are shown in chapter 7 with similar results.

The adopted photoionisation rate (again taken form Peter (1998)) appears quite unnatural with such a high rate that suddenly, at an arbitrary height, starts to work and ionises the gas totally. The results obtained with a more gradually growing ionisation rate are shown in section 7.2.3.

No absolute enrichment is obtained. In the H case the elements abundances present a small depletion (around 10%). The M case shows a stronger depletion($\approx$ 40%), while in the L case the hydrogen wind does not manage to transport the minor constituent out of the layer, and the density of the latter decays drastically by a factor of at least 10^{10}. These results are in strong contrast with the high enrichment obtained by Peter (1998).

When it comes to the relative abundance, the low FIP elements show some enrichment with respect to oxygen. In the H case the enrichment is about 10%, and in the M case it gets larger (between 30% and 50%), while the L case shows a strong depletion of many order of magnitude. Nevertheless the relative abundances are characterised by some rapid variations at the

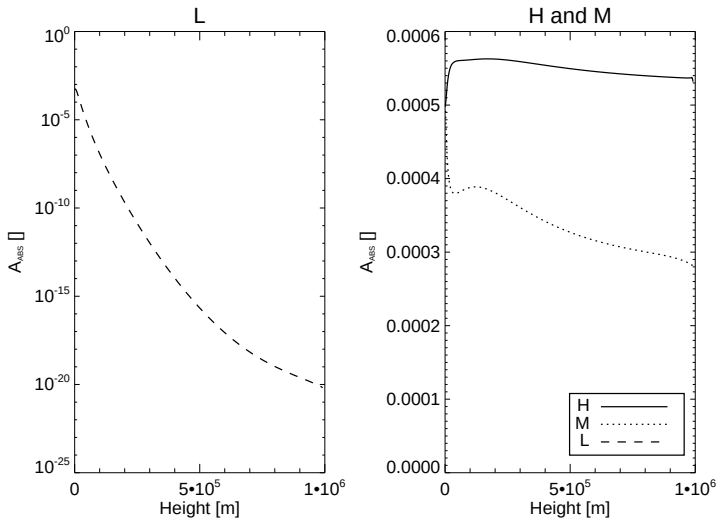

Figure 6.23: *The neon absolute abundance.*

lower boundary and the obtained relative enrichments are thus just artifacts, as it is shown with a further analysis in section 7.2.2.

6.4 Neon

The ionisation process for neon is strongly dominated by the radiative ionisation. The ratio between the collisional and the radiative ionisation rate, $\frac{C_{ni}}{R_{ni}}$, varies between 10^{-11} at the bottom to 10^{-5} at the top. The radiative recombination dominates the recombination process by factor larger than 10^6.

In order to reach the steady state the code is run for 2×10^6 s, 1×10^5 s and 1×10^4 s for the L, M and H case respectively.

6.4.1 Results

Fig. 6.23 shows the neon absolute abundance for the L case (left panel) and M and H cases (right panel). In the L case the absolute abundance falls radically by a factor of 10^{17}. Unlike the L case for oxygen and for the low FIP elements, the neon L case shows a monotonous, almost exponential behaviour throughout the slab. While the M case presents a decreasing absolute abundance the H case shows a rise of about 10% at lower altitude.

In Fig. 6.24 the neon relative abundances for the L case (left panel) and

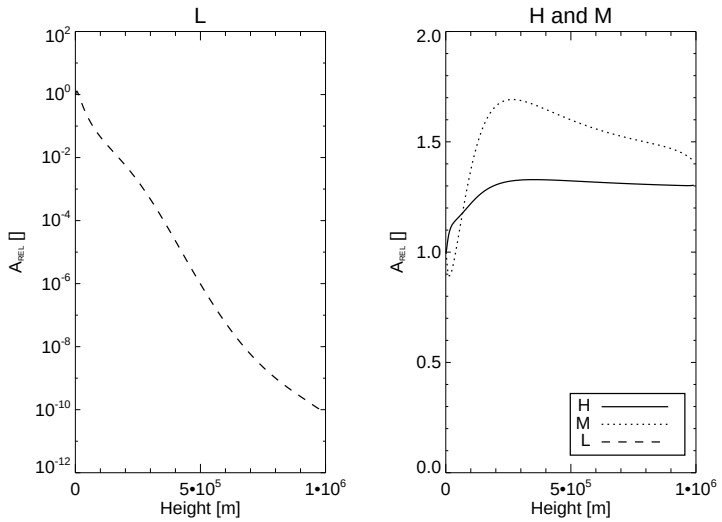

Figure 6.24: *The neon relative abundance.*

for the H and M cases (right panel) are shown. In the L case the relative abundance falls by a factor of 10^{10} while in the H and M case we have a relative enrichment by a factor of 0.3 and 0.5 respectively. The rise of the relative abundance happens in the lower part of the slab, up to $z \approx 2.5 \times 10^5$ m.

The neon ionisation degree is presented in Fig. 6.25. The L and M cases show an almost totally ionised gas already at the bottom of the slab. In the H case the *ionisation length* effect is visible and causes a delay in the ionisation degree with respect to the L and M cases. Thus, with the adopted radiative ionisation rate, neon gets fully ionised much before oxygen and hydrogen, despite that it has an ionisation energy of ≈ 22 eV relative to 13.6 eV for H and O.

The neutral and ionised neon velocities are shown in Fig. 6.26. As for the low FIP elements, because of the high ionisation degree, the NeI velocities are insignificant, except for the H case at the lower boundary. Here the NeI velocity is greater than the one of NeII. All the cases present a positive and monotonous ionised velocity.

Since neon is not fully ionised throughout the slab, and since the neutral velocities assume negative values, it is also interesting to study the neutral and ionised neon fluxes (Fig. 6.27). In the L case (left panel) the drastic density fall leads to almost zero fluxes, except at lower altitudes. Here neutral neon is streaming upward while ionised neon is falling. The M case (centre panel) shows a high upward ionised flux, while the neutral neon is streaming

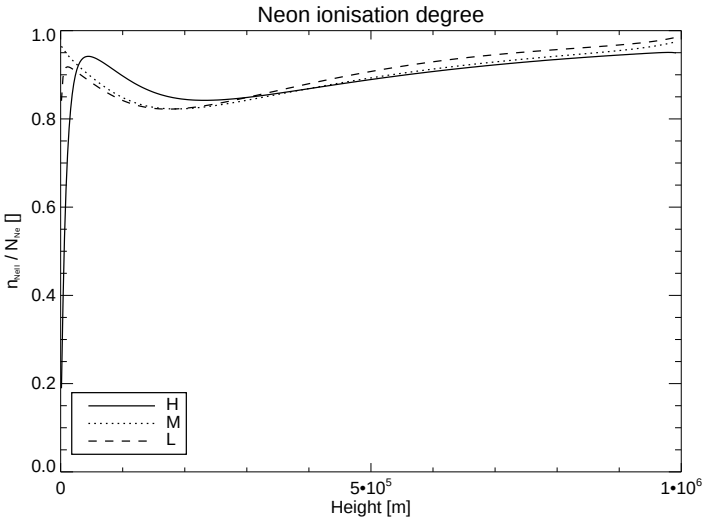

Figure 6.25: *The neon ionisation degree.*

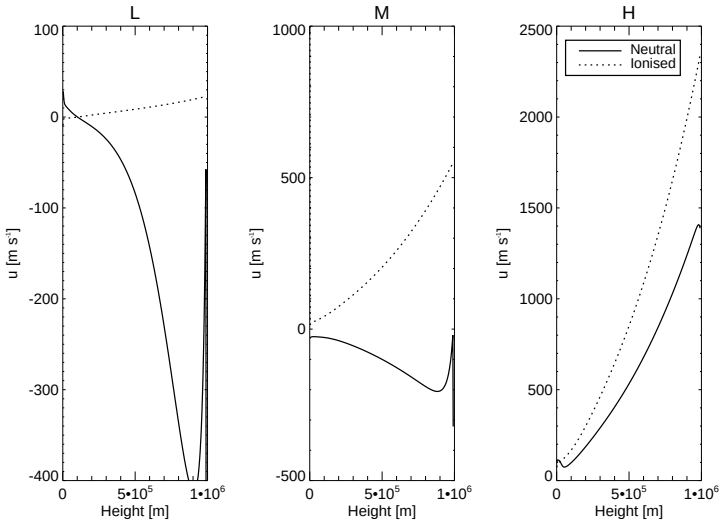

Figure 6.26: *The neutral and ionised neon velocity profiles.*

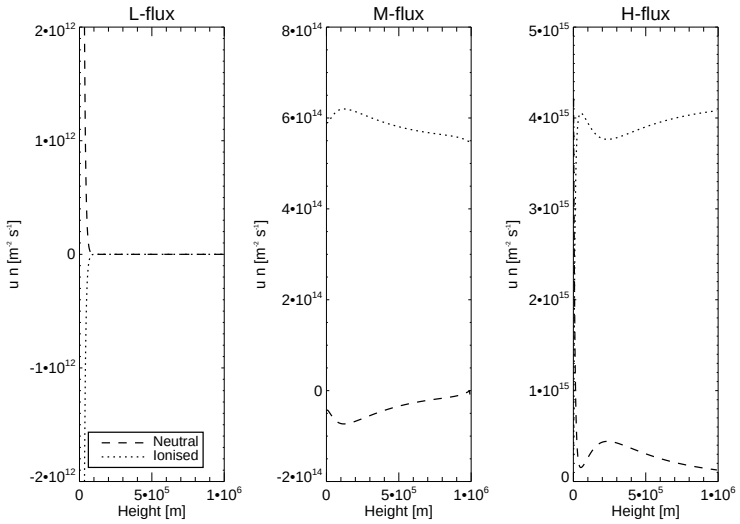

Figure 6.27: *The neutral and ionised neon fluxes.*

downward and constitutes a small part of the total flux at lower altitudes. In the H case (right panel) the neutral flux is slightly less significant and positive throughout the slab.

Fig. 6.28 shows the ratio between the neon and hydrogen relative velocity. For the H flux the ratio can appear slightly larger than one at the bottom, leading to a possible enrichment. In the L case the ratio is almost zero giving the net result that no neon is dragged up by hydrogen.

The force equilibrium for neutral and ionised neon in the H case is shown in Fig. 6.29. For NeI, the force equilibrium is characterised by a balance between gravity and collisions with hydrogen throughout the slab except for near the lower boundary. Here an upward pressure gradient force arises, balanced by the sum of gravity and collisions. At the very beginning of the layer, in order to balance the pressure gradient, the collision force becomes negative and the NeI velocities become thus higher than the hydrogen velocities. These high NeI velocities justify a Ne average velocity larger than hydrogen at the lower boundary. For NeII the picture is the same except at the lower boundary where a negative pressure gradient force is balanced by a high upward collisional force. To obtain such an upward force the NeII velocities must be lower than the hydrogen ones.

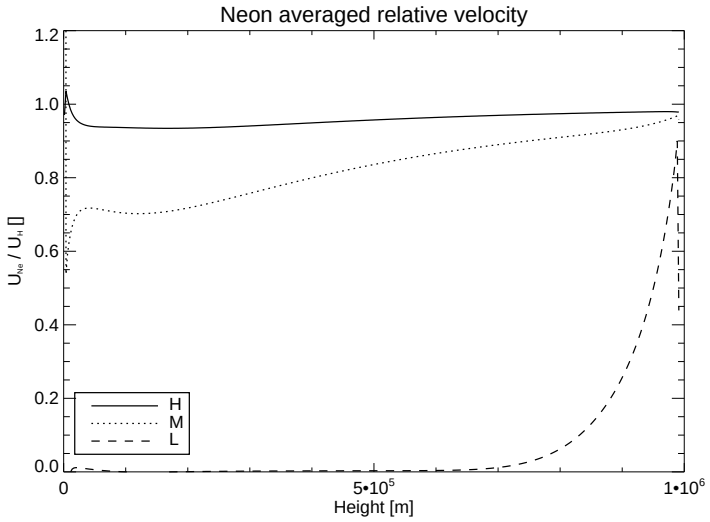

Figure 6.28: *The neon average velocity.*

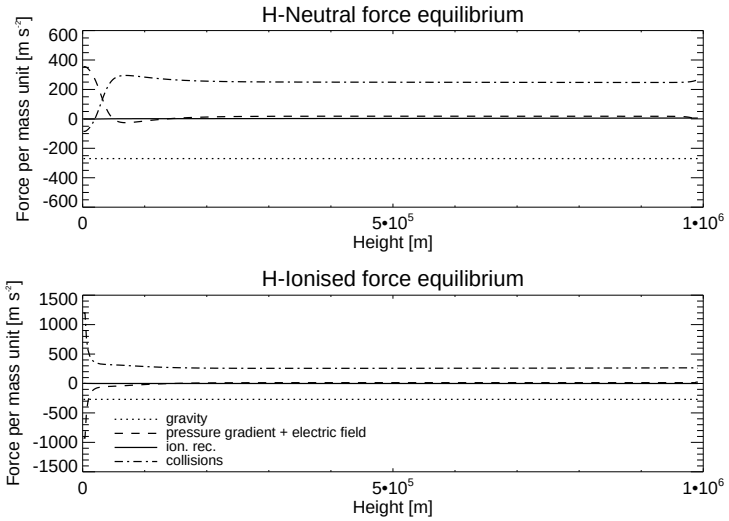

Figure 6.29: *H - Neon: The force equilibrium.*

6.4.2 Discussion

The H case for neon is quite interesting because the *ionisation length* effect is visible and a growing ionisation degree is achieved. This steep ionisation degree builds an upward pressure gradient force for NeI and a respective downward force for NeII. Since NeII is coupled to protons by a stronger collisional force the overall neon average velocity becomes larger than hydrogen. This velocity gives a very small (less than 10%) but visible absolute enrichment (if we do not account for the negative spike in the average velocity at the lower boundary).

Neon is a high FIP element and no enrichment should thus be obtained. This anomaly is probably due to the fact that in our model, using the ionisation rate by Peter (1998), neon gets ionised much before hydrogen. However this result shows that with a steep ionisation degree a small enrichment can be obtained. In section 7.2.1 we check the possibility to obtain such or maybe larger enrichment for the low FIP elements.

Chapter 7

Discussion

7.1 The background model

The results obtained in chapter 5 can be compared with the hydrogen background model of Peter and Marsch (1998). The largest difference between these models can be found in the choice of the boundary conditions. In Peter and Marsch (1998) the velocities for neutral and ionised hydrogen are forced to be equal not only at the top (as we do in our model) but also at the bottom. They give reasons for this choice by claiming that charge exchange and ionisation-recombination keep a tight collisional coupling between the charge states. As we have studied in eq. 5.7 an increasing ionisation rate leads to a velocity difference between the neutral and the ionised specie. Therefore forcing equal velocity at the bottom, where the ionisation rate increases, could be inappropriate. Another difference is that in our model we force a solar wind flux through the layer by a choice of the boundary conditions, while Peter and Marsch (1998) obtain such flux from the model itself. This means that in their model they claim that solar wind is a "product" of the chromosphere, whereas in our model the process that determines the solar wind mass flux is placed somewhere else above this chromospheric ionisation layer.

7.2 The minor constituents model

7.2.1 Searching for enrichment

Peter (1998) obtained a significant absolute fractionation for many minor constituents, whereas in this work no enrichment relative to hydrogen was found (except a small enrichment for one isolated case). The largest difference

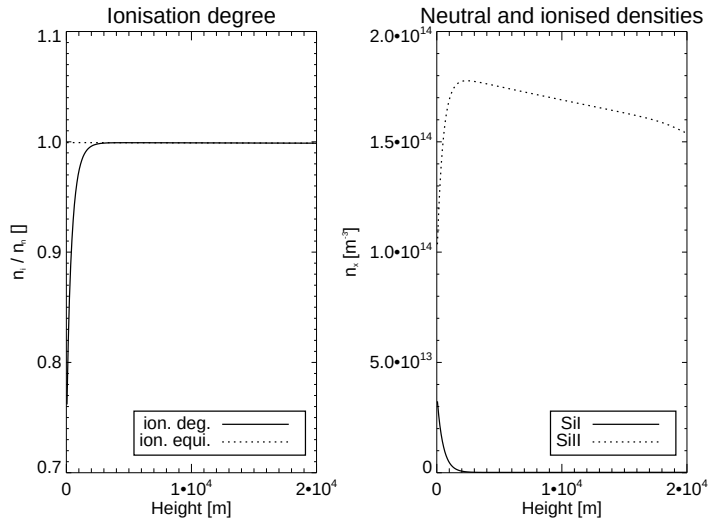

Figure 7.1: *The silicon ionisation degree(left panel) and the SiI together with SiII densities in H case, plotted for the ionisation area, using Peter's boundary conditions and a higher resolution grid.*

between Peter's approach and ours is represented by his coupling between the ionised and neutral minor constituent velocity, not only at the top but also at the bottom of the layer.

Another important aspect that needs more attention is the ionisation rate. The photoionisation rate from Peter (1998) (see section 2.1.1) for the minor constituents leads to a sudden and drastic ionisation. The respective ionisation length is therefore getting quite small. For example, silicon in the H flux case has $L_{ION} \approx 10^2$ m, that is 25 times smaller than the adopted grid spacing. Therefore in order to study this thin area, where the fractionation processes are believed to take place, a higher resolution grid (smaller grid spacing) is needed. We thus define a new grid where the grid points, instead of being distributed homogeneously, cover the ionisation area with a resolution that is higher than in the rest of the grid. In that way we are sure not to miss any important effect happening in the lower part of the grid.

We now want to study how and if (by using a higher resolution grid together with Peter's boundary conditions) any enrichment can really be obtained. The boundary conditions are thus modified as described above, both in the background and in the minority code. In the first part of the grid, up to $z = 2 \times 10^4$ m, the grid spacing is reduced by a factor of 100. We now present the results obtained for silicon in the H flux case.

The left panel of Fig. 7.1 shows the ionisation degree and the ionisation

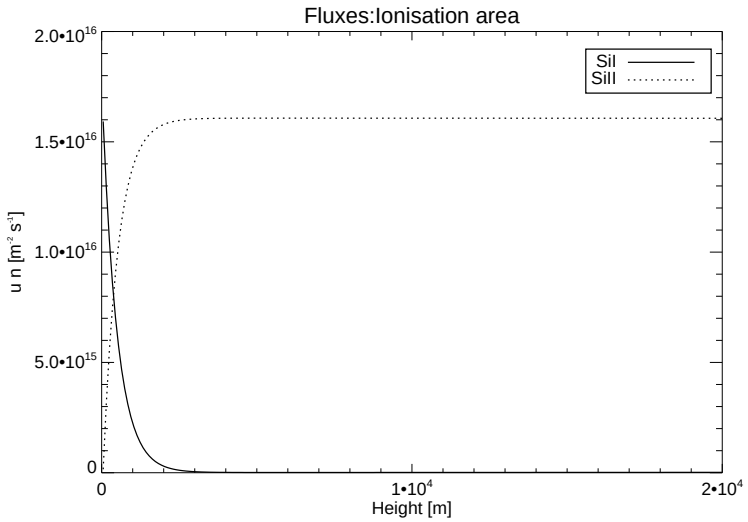

Figure 7.2: *The neutral and ionised silicon fluxes in the H case, plotted for the ionisation area, using Peter's boundary conditions and a higher resolution grid.*

equilibrium obtained for silicon near the lower boundary, while the right panel shows the SiI and SiII densities. Even if we use a grid spacing that is smaller than the theoretical ionisation length, and even if the in-streaming gas is only 1% ionised, silicon is highly ionised ($\approx 80\%$) already from the first grid point. However, a small *ionisation length effect* is visible at the very beginning of the layer.

The real effect of ionisation can be studied from the continuity equation, where we observe that in a steady state we have non-zero spatial derivatives of a particle flux only at those heights where the ionisation-recombination process is taking place. In other words, if the flux for SiI (or in the same way for SiII) does not show any spatial variation, the sum of the ionisation and recombination net effect is negligible. Analysing these fluxes, shown in Fig. 7.2, we see that the ionisation process is taking place from the lower boundary up to $z = 3 \times 10^3$ m. This means that the ionisation process is delayed as described by the *ionisation length* concept, but when it comes to the real ionisation degree, $n_{SiII}/(n_{SiI} + n_{SiII})$, this delay in ionisation is almost not visible.

A reason for this can be found in the SiI and SiII velocities at the bottom, displayed in Fig 7.3. At the lower boundary the velocities are forced to be equal, but already from the second grid point the two velocity profiles are separated by a huge gap. When the in-streaming neutral silicon gets ionised,

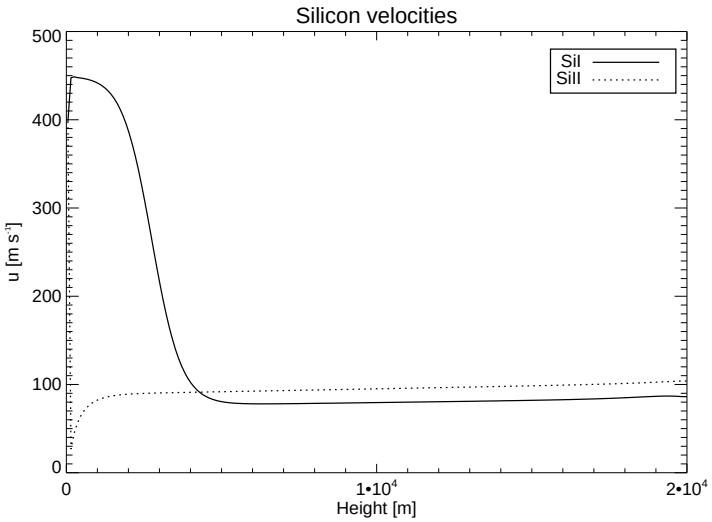

Figure 7.3: *The neutral and ionised silicon velocities in the H, plotted for the ionisation area, using Peter's boundary conditions and a higher resolution grid.*

its velocity falls to a near zero value, and then it increases slowly. In that way SiII can accumulate and the overall ionisation degree becomes as shown in Fig. 7.1 The ionisation delay due to the *ionisation length* concept is therefore strongly reduced. From this picture it also sounds quite unphysical to force the HI and HII velocities to be equal right where the ionisation takes place, because at those heights the pressure gradients for HI and HII give two opposite effects.

The force equilibrium is shown in detail in Fig. 7.4. The high SiI velocity at the bottom is caused by an upward pressure gradient force, which arises from a decreasing SiI density near the lower boundary. On the other hand SiII is subject to a downward pressure gradient force, balanced by the collisional friction. This pressure gradient is again caused by a SiII density increasing with height.

Finally, from Fig 7.5 we see that the average velocity for silicon at the lower boundary is greater than the hydrogen average velocity. Due to eq. 4.10, this leads to an enrichment that can also be observed as an increase in the absolute abundance from the lower boundary value of 5×10^{-4} to 6×10^{-4}.

Summarising this section, we have seen that even if we use a high enough precision in the grid we obtain a quite limited ionisation area where the minor constituent is already 80% ionised at the first grid point. This shows that

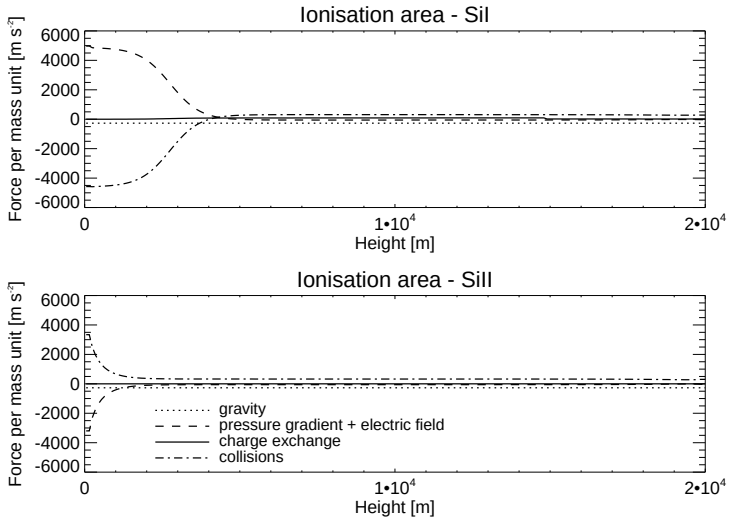

Figure 7.4: *The neutral silicon (upper panel) and ionised silicon (lower panel) force equilibrium in the H case, plotted for the ionisation area, using Peter's boundary conditions and a higher resolution grid.*

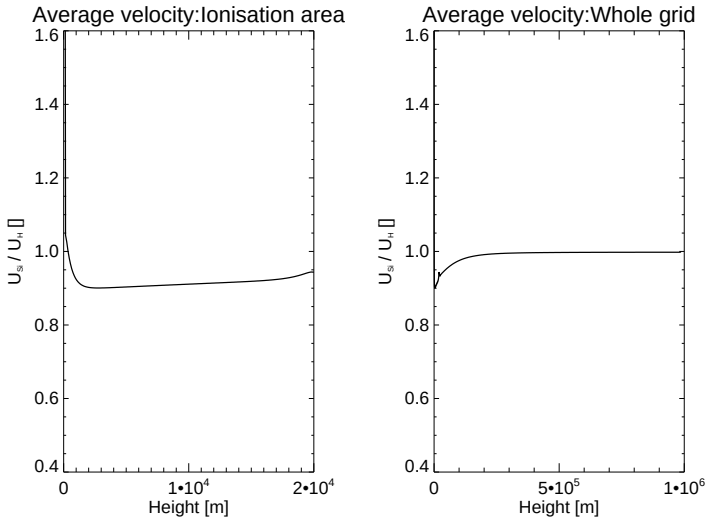

Figure 7.5: *The ratio between the silicon and the hydrogen average velocity, plotted for the ionisation area (left panel) and for the whole grid (right panel) in the H case,using Peter's boundary conditions and a higher resolution grid.*

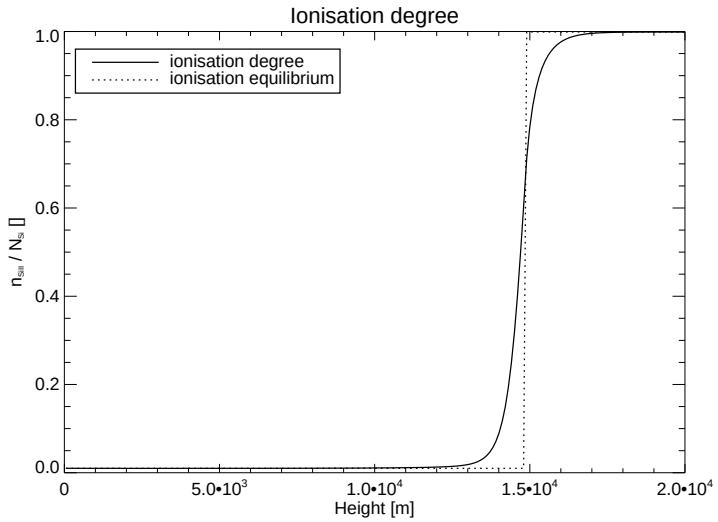

Figure 7.6: *The silicon ionisation degree and ionisation equilibrium plotted for the ionisation area.*

the *ionisation length* simplification, used as a fundamental process by Peter (1998), does not give a correct picture of the ionisation dynamic. However, the remaining 20% of the ionisation process manages to build a pressure gradient that increases the average velocity of the minor constituent up to a value a bit higher than the hydrogen average velocity, leading to a very small enrichment.

7.2.2 Additional results

We now want to verify if the very small enrichment obtained in the previous section is a real process that can explain the FIP effect, or if it only is an event that depends on the choice of some parameters like the boundary conditions. We move the ionisation area up to a height of $z_{ion} = 1.5 \times 10^4$ m by turning on the photoionisation rate for minor constituents at $z = z_{ion}$ instead of at the lower boundary $z = 0$ m. This allows us to study what happens below the radical increase of the photoionisation rate, and the solution we obtain is less dependent of an arbitrary choice for the boundary conditions.

The results for the H flux case for silicon, with the described modifications and with our boundary conditions, are presented below.

Fig. 7.6 shows the ionisation degree for silicon, plotted together with the ionisation equilibrium (see eq. 5.4). The latter, following the photoionisation rate, has a constant value of 1% from the lower boundary up to $z = 1.5 \times 10^4$

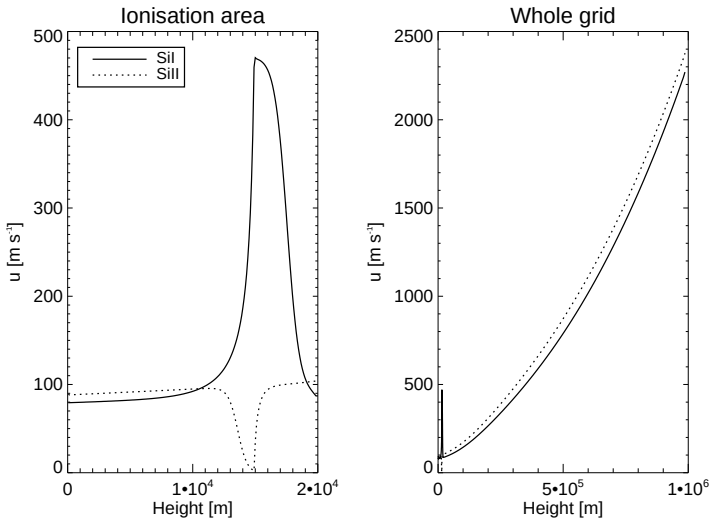

Figure 7.7: *The neutral and ionised silicon velocities, plotted for the ionisation area (left panel) and for the whole grid (right panel).*

m, where it makes a discrete jump increasing to 100% and it then keeps this value for the rest of the grid. The actual ionisation degree shows a smoother behaviour. Its value is higher than equilibrium value below the height of the photoionisation "ignition" and lower than the equilibrium value above this height.

We note that Fig. 7.1 is quite similar to Fig. 7.6 if we shift the latter to the left by a distance $\Delta z = 1.5 \times 10^4$ m.

By studying the SiI flux we can measure the ionisation length, obtaining $L_{ION} \approx 2 \times 10^2$ m. However, the real length (and time) needed by the gas to become half ionised, is much larger ($\approx 4 \times 10^3$ m). This is caused by the dynamic following a high velocity difference between neutral and ionised silicon, as shown in Fig. 7.7.

The neutral silicon velocity shows a sudden rise followed by a similar fall, located at the height of the rate ignition, whereas the ionised silicon velocity has a smaller magnitude dip at the same height. These features do not influence the velocities for the rest of the grid, where both the SiI and SiII velocities increase at the same rate. The ionisation process thus appears just as a local event that does not modify the velocity at the top (or at the bottom) of the grid. Furthermore, this result is in agreement with what we found with the old grid (see right panel of Fig. 6.12), except for the magnitude of the spike near the lower boundary, and therefore legitimates the results of chapter 6.

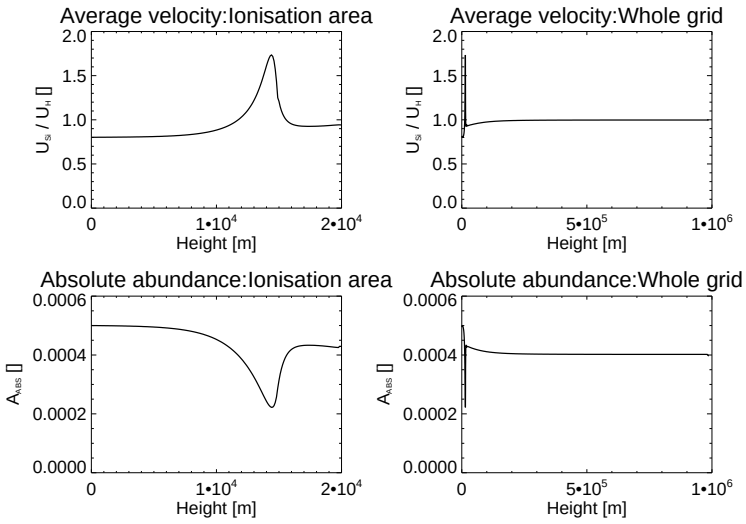

Figure 7.8: *The ratio between the silicon and the hydrogen average velocity (upper panels), plotted for the ionisation area (left panel) and for the whole grid (right panel).*

The ratio between the silicon and hydrogen average velocity is shown in the upper panels of Fig. 7.8. The sum of the SiI and SiII velocities gives a positive rise in the average velocity. However, as already mentioned, this feature does not modify the overall velocity behaviour (right panel). Hence, except for the ionisation area, the silicon average velocity is less than the hydrogen velocity, also at the bottom of the grid. This means that a real fractionation process does not take place, but rather a local depletion.

The overall absolute abundance shows a depletion from the lower boundary value 5×10^{-4} to a value 4×10^{-4} at the top of the grid. This is due to flux conservation and the increasing of silicon velocities. In fact, before a full coupling between silicon and hydrogen is reached, the silicon velocities are lower than the hydrogen velocities. Also the dip in the absolute abundance proceeds from the total flux conservation and from the average velocity profile. The latter can be understood by studying the force equilibrium shown in Fig. 7.9.

The force equilibrium for SiI in the ionisation area (upper left panel of Fig. 7.9) presents a high pulse of the pressure gradient caused by the decreasing SiI density in the ionisation process. This upward pressure gradient force leads to an increase of the SiI velocities. A collisional friction with the hydrogen background therefore arises and balances this pressure gradient. For SiII the force balance (lower left panel of Fig. 7.9) shows an opposite symmetry,

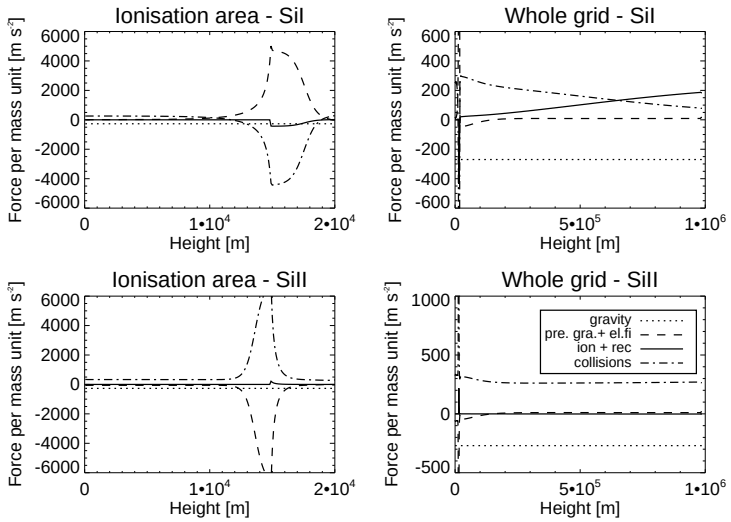

Figure 7.9: *The neutral silicon (upper panels) and ionised silicon (lower panels) force equilibrium, plotted for the ionisation area (left panel) and for the whole grid (right panel).*

with a downward pressure gradient force balanced by a positive collisional friction. Even if the pressure gradients for SiI and SiII are of the same order of magnitude we have seen that the sudden decrease in the SiII velocities is smaller than the respective increase in the SiI velocity. This is caused by the far more efficient Coulomb collisions between SiII and protons that manage to balance the pressure gradient with a lower velocity difference between the minor constituent and the background. Gravity is negligible in the ionisation area.

Another important result, achieved with this new grid, concerns the relative abundance, i.e. the silicon abundance relative to oxygen, shown in Fig. 7.10 (upper panels). Except from the ionisation area, which again does not influence the rest of the grid, the silicon abundance remains constant relative to oxygen. This result is confirmed by the ratio between silicon and oxygen average velocities, shown in the lower panel of Fig. 7.10. Even if the velocity ratio shows a spike in the ionisation area, the silicon average velocity at the lower boundary is not larger than the oxygen average velocity. This means that no relative enrichment for silicon is obtained. This result is in contrast with what we showed in Fig. 6.10 (right panel), where an enrichment relative to oxygen was achieved. The discrepancy is due to the different location of the ionisation rate's "ignition point", and proves that we lose critical information concerning what happens at lower altitudes if we place this "ignition

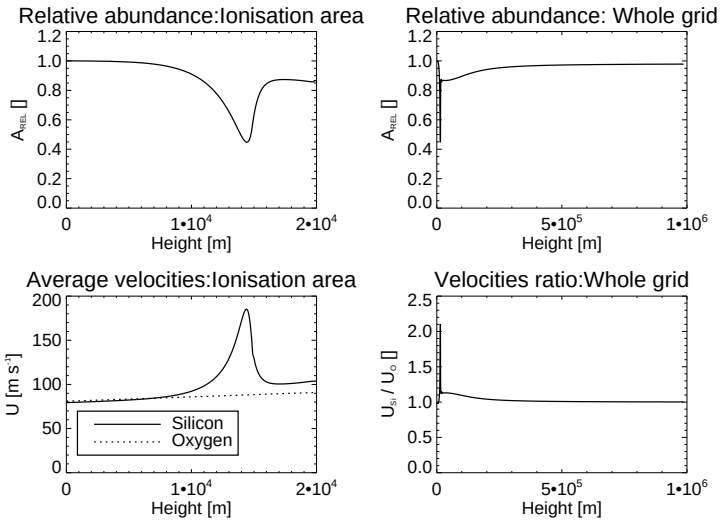

Figure 7.10: *The silicon relative abundance (upper panels) plotted for the ionisation area (left panel) and for the whole grid (right panel). The silicon and oxygen average velocities (lower panels) in the ionisation area. The ratio between silicon and oxygen average velocities for the whole grid (right panel).*

point" at the lower boundary.

In this section we have seen that a steep ionisation degree leads to a fall in the abundance, located exactly at the ionisation height z_{ion}, followed immediately by an analog rise of the abundance. This means that the abundance variations measured with respect to this low value can appear like an enrichment (see previous paragraph), but at the same time these ionisation area abundance values are depleted with respect to photospheric values (represented by the lower boundary). No real enrichment is therefore achieved. In other words, because the ionisation process causes a local density depletion, comparing abundance values from higher altitudes with the abundance value at z_{ion} will give an unreal enrichment.

The area where the minor constituent velocity exceeds the hydrogen velocity is characterised by a pressure gradient force due to the ionisation process. Below this area no force can provide for such a high velocity. Since collisions constitute the only force that balances gravity, the minor constituent average velocity must be lower than the hydrogen velocity, both above and below the ionisation area.

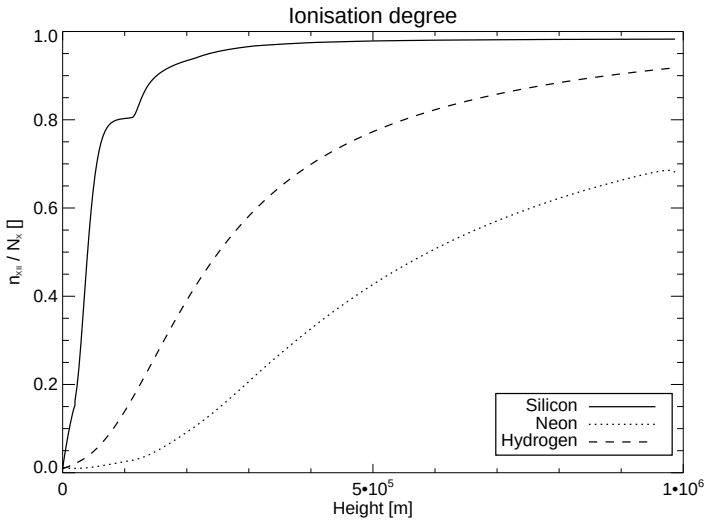

Figure 7.11: *A gradually growing ionisation degree for silicon, hydrogen and neon, in the H flux case.*

7.2.3 Gradual ionisation

As already mentioned (see section 6.3.4), the adopted photoionisation rate, characterised by a sudden and drastic increase, is quite unphysical. This ionisation is caused by radiation coming from the above corona, but the ionising radiation stops to work at the lower boundary or at a so-called "ignition point", and no gas is ionised below this wall.

We now want to check if any fractionation process can be obtained with a more likely ionisation degree. We build a gradual ionisation rate and run the code for the H case for silicon, oxygen and neon. Fig. 7.11 shows the gradually growing ionisation degree for silicon and neon, compared with hydrogen. With the new ionisation rate silicon becomes ionised before hydrogen while neon becomes ionised after it.

Fig. 7.12 shows the average velocity of silicon and neon relative to hydrogen (left panel), and relative to oxygen (right panel), in the H flux case. The value, ≈ 0.8, of the average silicon velocity relative to hydrogen at the lower boundary leads to a depletion in absolute abundance by 20%, while the absolute neon abundance is depleted by a factor of 40%. These values confirm what we found in section 7.2.2, and show that also with a gradual ionisation no enrichment is obtained. When it comes to the relative abundance, silicon has the same velocity as oxygen at the lower boundary and thus no enrichment is obtained, even if the earlier ionisation of silicon causes a rise,

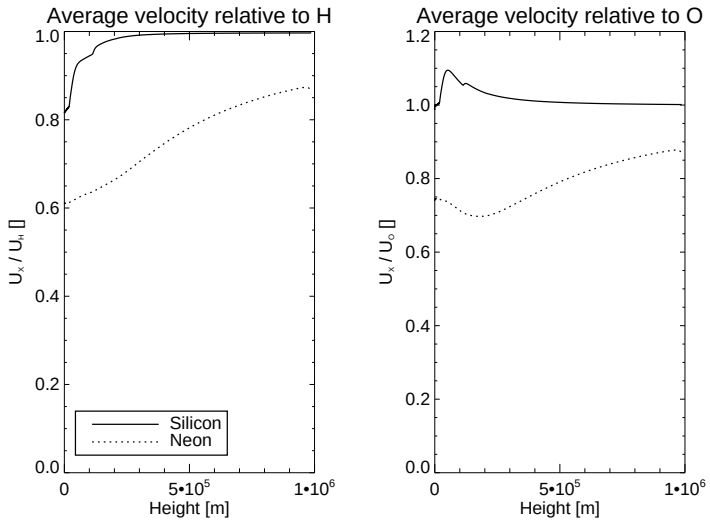

Figure 7.12: *Si and Ne average velocities relative to hydrogen (left panel) and to oxygen (right panel), for the H flux case with a gradual ionisation.*

followed by a similar fall, in the average velocity (repeating the pattern seen in section 7.2.2). The ratio between the neon and oxygen average velocities shows that neon is depleted by 20% with respect to oxygen.

In conclusion, we have seen in this section that with a gradually growing ionisation degree, no enrichment for the low FIP elements can be obtained. Moreover, the high FIP element neon is depleted relative to both hydrogen and oxygen.

Chapter 8

Summary

In-situ observations together with spectroscopic measurements show that the elemental composition of the solar atmosphere varies from the photosphere to solar wind. An enrichment by a factor of 2 or more for the low FIP elements relative to oxygen (and with larger uncertainty also relative to hydrogen) has been found.

Many models have been implemented in order to explain this fractionation. In this work we have followed the same approach as Peter (1998) and tried to repeat his results concerning the FIP effect in fast solar wind.

A background model that describes a layer of the chromosphere where hydrogen is the only constituent, has been implemented. The obtained results for the hydrogen background are substantially in agreement with Peter and Marsch (1998), who provide the background model for Peter (1998).

A second model that describes minor constituents in such a background has also been made. This minor constituent model has been run for different parameter values (like the wind flux) and with different boundary conditions.

No enrichment comparable to the ones achieved by Peter (1998) has been found for the low FIP elements. A downward pressure gradient force arises and brakes the ionised specie so that this can pile up at the lower boundary and oppose the formation of a steep ionisation degree. However, if a steep enough ionisation degree is somehow built at the lower boundary, an upward pressure gradient force acting on the neutral specie can arise. In that way a small enrichment, definitively smaller than the results of Peter (1998), is obtained.

Furthermore, a new and perhaps more important result have been obtained by moving the ionisation area away from the lower boundary: at the ionisation height the minor constituent abundance reaches a local minimum. It is therefore incorrect to adopt this minimum as the reference photospheric value when evaluating the enrichment.

This result is just the validation of a simple physical line of reasoning. In order to transport these heavy ions out of the gravitational field an upward force able to balance gravity is needed. If this force is represented by collisions with hydrogen the minor constituent velocity must be lower than the hydrogen velocity, and no enrichment can be obtained. If instead this upward force is constituted by the pressure gradient force caused by the ionisation process, no high velocity will be obtained outside the ionisation area, and hence no real enrichment can be obtained. Let's say that the ionisation process provides the minor constituent with this upward force (that drives the trace gas with a velocity higher than hydrogen). In order to keep this high velocity and thus obtain a real enrichment, a pressure gradient able at least to balance gravity must arise all the way down from the ionisation area to the photosphere. In such a way, because of the large height scale of the minor constituent, the density will drop so much that almost no particles will be left in the solar wind.

This work has thus confirmed that the ionisation-diffusion process suggested by Peter (1998) as a pure steady-state mechanism, cannot account for the observed FIP effect in the solar wind.

A further work could study a time-dependent process where a regularly repeated mixing keeps the chromospheric abundance at photospheric values. It is necessary to investigate how this mixing process can interact with the ionisation-diffusion mechanism and whether or not an enrichment of the low FIP elements can be achieved.

A l'alta fantasia qui mancò possa;
ma già volgeva il mio disio e 'l velle,
sì come rota ch'igualmente è mossa,
l'amor che move il sole e l'altre stelle.

Here vigour failed the lofty fantasy:
But now was turning my desire and will,
Even as a wheel that equally is moved,
The Love which moves the sun and the other stars.
Dante Alighieri

Bibliography

Abramowitz, M. and Stegun, I. A. (1964). *Handbook of mathematical functions*. U.S. Department of Commerce, third edition.

Arnaud, M. and Raymond, J. (1992). Iron ionization and recombination rates and ionization equilibrium. *ApJ*, 398:394–406.

Arnaud, M. and Rothenflug, R. (1985). An updated evaluation of recombination and ionization rates. *A&AS*, 60:425–457.

Asplund, M., Grevesse, N., Sauval, A. J., Allende Prieto, C., and Kiselman, D. (2004). Line formation in solar granulation. IV. [O I], O I and OH lines and the photospheric O abundance. *A&A*, 417:751–768.

Banks, P. M. and Kockarts, G. (1973). *Aeronomy*. Academic Press, Inc. New York.

Byhring, H. S., Esser, R., and Lie-Svendsen, Ø. (2008). The Funnel Geometry of Open Flux Tubes in the Low Solar Corona Constrained by O VI and Ne VIII Outflow. *ApJL*, 673:L91–L94.

Feldman, U. and Laming, J. M. (2000). Element Abundances in the Upper Atmospheres of the Sun and Stars: Update of Observational Results. *Physica Scripta*, 61:222–+.

Gray, D. F. (2005). *The observation and analysis of the stellar atmospheres*. Cambridge University Press, New York.

Grevesse, N. and Sauval, A. J. (1998). Standard Solar Composition. *Space Science Reviews*, 85:161–174.

Henoux, J. C. and Somov, B. V. (1997). The photospheric dynamo. I. Physics of thin magnetic flux tubes. *A&A*, 318:947–956.

Hummer, D. G. (1983). The generalized exponential-integral. *Journal of Quantitative Spectroscopy and Radiative Transfer*, 30:281–287.

Korevaar, P. and van Leer, B. (1988). Time-dependent corona models - A numerical method. *A&A*, 200:153–167.

Marsch, E., von Steiger, R., and Bochsler, P. (1995). Element fractionation by diffusion in the solar chromosphere. *A&A*, 301:261–+.

Peter, H. (1998). Element fractionation in the solar chromosphere driven by ionization-diffusion processes. *A&A*, 335:691–702.

Peter, H. and Marsch, E. (1998). Hydrogen and helium in the solar chromosphere: a background model for fractionation. *A&A*, 333:1069–1081.

Press, W., S.A.Teukolsky, Vetterling, W., and Flannery, B. (1992). *Numerical Recipes in Fortran 77*. Cambridge University Press.

Russell, H. N. (1929). On the Composition of the Sun's Atmosphere. *ApJ*, 70:11–+.

Schultz, D. R., Krstic, P. S., Lee, T. G., and Raymond, J. C. (2008). Momentum Transfer and Viscosity from Proton-Hydrogen Collisions Relevant to Shocks and Other Astrophysical Environments. *ApJ*, 678:950–960.

Schunk, R. W. (1977). Mathematical structure of transport equations for multispecies flows. *Reviews of Geophysics and Space Physics*, 15:429–445.

Shull, J. M. and van Steenberg, M. (1982). The ionization equilibrium of astrophysically abundant elements. *ApJS*, 48:95–107.

Vauclair, S. (1996). Element segregation in the solar chromosphere and the FIP bias: the "Skimmer" model. *A&A*, 308:228–232.

Vernazza, J. E., Avrett, E. H., and Loeser, R. (1981). Structure of the solar chromosphere. III - Models of the EUV brightness components of the quiet-sun. *ApJS*, 45:635–725.

von Steiger, R. and Geiss, J. (1989). Supply of fractionated gases to the corona. *A&A*, 225:222–238.

von Steiger, R. and Schwadron, N. A. (2000). Solar Wind Composition. In Ramaty, R. and Mandzhavidze, N., editors, *High Energy Solar Physics Workshop - Anticipating Hess!*, volume 206 of *Astronomical Society of the Pacific Conference Series*, pages 54–+.

von Steiger, R., Schweingruber, R. F. W., Geiss, J., and Gloeckler, G. (1995). Abundance variations in the solar wind. *Advances in Space Research*, 15:3–.

Wang, Y.-M. (1996). Element Separation by Upward Proton Drag in the Chromosphere. *ApJL*, 464:L91+.